Extreme Birkeland currents are more likely during geomagnetic storms on the dayside of the Earth

John C. Coxon[1], Gareth Chisham[2], Mervyn P. Freeman[2], Colin Forsyth[3], Maria-Theresia Walach[4], Kyle R. Murphy[1], Sarah K. Vines[5], Brian J. Anderson[5], Andrew W. Smith[1], Alexandra R. Fogg[6]

[1]Department of Mathematics, Physics and Electrical Engineering, Northumbria University, Newcastle upon Tyne, UK

[2]British Antarctic Survey, Cambridge, UK

[3]Mullard Space Science Laboratory, UCL, Dorking, UK

[4]Lancaster University, Lancaster, UK

[5]Johns Hopkins University Applied Physics Laboratory, Laurel, MD, USA

[6]School of Cosmic Physics, DIAS Dunsink Observatory, Dublin Institute for Advanced Studies, Dublin, Ireland

Key Points:

- Geomagnetic storms are more likely than substorms to drive extreme field-aligned current densities
- Extreme current densities are most likely on the dayside and least likely within three hours of midnight
- The highest probabilities of extreme current densities occur in Region 2 currents during geomagnetic storms

Corresponding author: John C. Coxon, work@johncoxon.co.uk

Abstract

We examine the statistical distribution of large-scale Birkeland currents measured by the Active Magnetosphere and Planetary Electrodynamics Response Experiment (AMPERE) in four unique categories of geomagnetic activity for the first time: quiet times, storm times, quiet-time substorms, and storm-time substorms. A novel method is employed to sort data into one of these four categories, and the categorisations are provided for future research. The mean current density is largest during substorms and its standard deviation is largest during geomagnetic storms. Current densities which are above a low threshold are more likely during substorms, but extreme currents are far more likely during geomagnetic storms, consistent with a paradigm in which geomagnetic storms represent periods of enhanced variability over quiet times. We demonstrate that extreme currents are most likely to flow within the Region 2 current during geomagnetic storms. This is unexpected in a paradigm of the current systems in which Region 1 current is generally larger.

Plain Language Summary

We take measurements from a set of 66 spacecraft orbiting Earth to look at electric currents that flow along Earth's magnetic field lines. We look at different types of space weather called "geomagnetic storms" and "substorms", and combine methods to detect when those types of space weather happen. We use our combined method to separate our measurements into the different types of space weather, and then we look at how strong the currents are during each type of space weather. We plot histograms of the strengths and then use those histograms to work out the underlying mathematics of the strengths: we can then plot further graphs showing how those underlying mathematics change. We then work out when the very strongest currents are likely to flow, and during which type of space weather this occurs, which is useful both for understanding the system and for mitigating against the risks of space weather.

1 Introduction

Geomagnetic storms and substorms represent two of the most important modes of variability in solar wind-magnetosphere-ionosphere coupling. Substorms were first codified by Akasofu (1964), who described the expansion and recovery phases of the sub-

storm; the growth phase was described later (McPherron, 1970) and the link between substorms and Interplanetary Magnetic Field (IMF) B_Z observed later still (Kokubun, 1972). In the growth phase, dayside magnetic reconnection adds magnetic flux to the polar cap, and newly opened flux convects over the poles to the nightside, into the magnetotail (e.g. Baker et al., 1996) during intervals of enhanced solar wind-magnetosphere coupling (Dungey, 1961; Siscoe & Huang, 1985; Cowley & Lockwood, 1992). Flux loading in the magnetotail leads to thin current sheets conducive to nightside magnetic reconnection closing flux in the magnetotail (e.g. Sergeev et al., 2011; Sitnov et al., 2019) which occurs during the expansion phase of a substorm. Substorms typically occur after periods of southward IMF B_Z (Freeman & Morley, 2009) and exhibit extreme geomagnetically induced current (GIC) behaviour (Freeman et al., 2019).

Different substorm identification methods are based on methods such as auroral imaging (e.g. Frey et al., 2004) or high-latitude ground magnetometer observations (e.g. Newell & Gjerloev, 2011) and provide the user with a list of times at which substorms have occurred. This enables superposed epoch analyses, which have been used extensively to examine the behaviour of the system during substorms (e.g. Walach & Milan, 2015; Walach et al., 2017). Birkeland currents have also been extensively examined during substorms (e.g. Billett et al., 2020; Clausen, Milan, et al., 2013; Clausen, Baker, et al., 2013; Ebihara & Tanaka, 2023; Imajo et al., 2020; Murphy et al., 2012). Case studies of storm-time substorms have shown that both R1 and R2 current are intensified during these events (Mishin et al., 2020), consistent with substorms generally (Coxon et al., 2014b, 2017), although it has also been shown that Birkeland currents are highly filamentary in both substorms (Forsyth et al., 2014) and storm-time substorms (Nakamura et al., 2016). Recently, the Substorm Onsets and Phases of the Electrojet (SOPHIE) technique (Forsyth et al., 2015) provides a method to identify the start (and therefore the end) of every substorm phase. This dataset allows for a time series to be categorised by whether any given timestamp is in a substorm, and in which phase; it has been exploited in various statistical studies (e.g. Forsyth et al., 2016; Coxon, Freeman, et al., 2018).

Geomagnetic storms have been well-examined for decades (Chapman & Bartels, 1940; Akasofu et al., 1963), preceded by study of what were simply called magnetic storms over a century ago (Birkeland, 1908, 1913; Chapman & Ferraro, 1931). Gonzalez et al. (1994) note that it was once thought that these storms were simply collections of substorms, but suggest that storms and substorms are interrelated but distinct phenomena.

The Dst index has been used extensively to understand storm dynamics (Akasofu et al., 1963), as geomagnetic storms lead to a build up of the ring current which in turn causes characteristic signatures in the equatorial ground magnetometers used to produce the Dst index. Yokoyama & Kamide (1997) argued that the intensity of the storm is linked to its duration. Strong IMF B_Z is a good predictor of a geomagnetic storm (Kokubun, 1972; Burton et al., 1975; Gonzalez & Tsurutani, 1987; Tsurutani et al., 1992; Loewe & Prölss, 1997), while solar wind pressure is more relevant than B_Z for storm sudden commencements (Taylor et al., 1994). During geomagnetic storms, the enhanced ring current retards the onset of nightside reconnection and thus the onset of substorms, allowing the auroral oval to reach larger sizes prior to substorm expansion phase onset (Milan, Grocott, et al., 2009; Milan, Hutchinson, et al., 2009; Milan, 2009). Recently, it has been demonstrated that storm times are vital to understanding extreme GIC signatures (Smith et al., 2019, 2021), and work has been done to explore Birkeland currents during geomagnetic storms (e.g. Kleimenova et al., 2021; Lukianova, 2020a,b; Maute et al., 2021; Ovodenko et al., 2020; Pedersen et al., 2021, 2022, 2023).

Hutchinson et al. (2011) developed a method to algorithmically identify the individual phases (initial, main, and recovery phases) of geomagnetic storms, finding that the duration of the main phase increased with storm intensity up to a point but then started to decrease again, which they argued was contrary to Yokoyama & Kamide (1997). This method was adapted by Walach & Grocott (2019), who made a small change to the way the start of the main phase is determined and investigated convection patterns during geomagnetic storms. Murphy et al. (2018) presented a storm list which was defined in terms of storm peak (i.e., minimum Dst) and the start and end of the storm. These more recent lists allow for a time series to be categorised by whether or not any given timestamp is in a geomagnetic storm, and timestamps can be further subdivided by storm phase.

Field-aligned currents, proposed by Birkeland (1908, 1913) and known as Birkeland currents, are an important component of solar wind-magnetosphere-ionosphere coupling, especially during active intervals of geomagnetic storms and substorms. They are known to chiefly comprise two rings of current which encircle the geomagnetic pole, offset towards the nightside (Iijima & Potemra, 1978): Region 1 (R1) on the poleward side and Region 2 (R2) on the equatorward side. R1 is upward on the dusk side of the polar cap and downward on the dawn side, and R2 vice versa. There are other Birkeland

currents: NBZ currents flow during northward IMF, hence their name, and are observed poleward of R1 (Iijima et al., 1984; Zanetti et al., 1984). Cusp currents are also observed poleward of R1 during southward IMF, and have morphology determined by IMF B_Y (Iijima & Potemra, 1976b; Saunders, 1989). Further high-latitude currents were reported as mantle currents, associated with antisunward convection flows and the velocity shear as they crossed the polar cap (Ohtani et al., 1995a,b). Ohtani et al. (1995b) noted that 'The term "region 0" has been used in the past to refer to any FAC system poleward of region 1 currents', but it seems that cusp and mantle currents are driven by different physical mechanisms.

The Active Magnetosphere and Planetary Electrodynamics Response Experiment (AMPERE) provides measurements of Birkeland currents from 2010 onwards based on magnetometer measurements from the Iridium Communications Network constellation (Anderson et al., 2000, 2021; Waters et al., 2001, 2020). Iridium data were used to study Birkeland currents during two geomagnetic storms (Anderson et al., 2002), concluding that the Birkeland current systems intensified and moved equatorward with southward IMF B_Z during geomagnetic storms, and that they moved equatorward more quickly when the solar wind pressure was higher in storms: this has been shown statistically (Coxon et al., 2014a,b; Carter et al., 2016). AMPERE was used by Coxon et al. (2016) to show that the Birkeland currents in the Northern Hemisphere are typically stronger than those in the Southern Hemisphere (Laundal et al., 2017; Coxon et al., 2022) and has also been used to explore the timescales of Birkeland currents during solar wind driving (Anderson et al., 2014; Coxon et al., 2019; Forsyth et al., 2018; Milan et al., 2018; Shore et al., 2019; Kunduri et al., 2020). A review of magnetospheric currents and their generation in solar wind-magnetosphere-ionosphere coupling was conducted by Milan et al. (2017) and a review of research with AMPERE was presented in Coxon, Milan, & Anderson (2018).

In this paper, we follow on from work on the underlying probability distributions of Birkeland current densities. Super Dual Auroral Radar Network (SuperDARN) data have been used to obtain ionospheric vorticities which are closely related to Birkeland currents (Sofko et al., 1995; McWilliams et al., 2001; Chisham et al., 2009). These data were used by Chisham & Freeman (2010) to show that the distributions of vorticity magnitude had more kurtosis than normally-distributed quantities (they were leptokurtic). Chisham & Freeman (2021) fit q-exponential functions to the distributions to obtain the

survival function of the distributions, and therefore the probabilities of observing extreme values of ionospheric vorticity.

Coxon et al. (2022) performed a similar analysis on AMPERE-derived Birkeland currents from 2010–2012, and found that they are also well-described by a q-exponential distribution. They found that the probability of current densities above a given threshold was higher in the Northern Hemisphere than in the Southern for currents at multiple amplitude thresholds, and that the disparity was greater at larger thresholds. They also found that extreme currents were most probable in the average R2 current region on the dayside, at a colatitude of $18° - 22°$, but had the sense of the average R1 current on the dayside. They identified two paradigms which could explain the results:

1. Extreme currents occur in R1 at the point when the current ovals are most expanded. Counter-intuitively, this means that the underlying distribution of the R1 current system changes as the polar cap expands.
2. Extreme currents occur in R2 due to closure through an intensified ring current during geomagnetic storms. Counter-intuitively, this means that extreme R2 currents occur in the opposite sense to the R2 current system.

Coxon et al. (2022) did not conclusively show which paradigm was responsible for their results, noting that both paradigms might play a role and highlighting that filamentary currents may also be a factor (Forsyth et al., 2014; Nakamura et al., 2016; Liu et al., 2021). Building on the work of Coxon et al. (2022), we break down the distributions of Birkeland currents by storm or substorm phase to examine how large-scale geomagnetic activity impacts on the occurrence of extreme Birkeland currents. We define four categories based on whether a timestamp is within a storm, a substorm, both, or neither. We then subdivide the AMPERE dataset according to the different categories (Section 2), demonstrating that the mean current density is generally larger during substorms but that the standard deviation is generally larger during storms (Section 3). In Section 4, we examine the probability of low, high, and extreme currents and find that extreme currents are most likely to be observed during storm times and storm-time substorms on the dayside of Earth. We then subdivide into R1 and R2 current regions to resolve the ambiguity between the paradigms described above.

2 Birkeland currents in different event categories

We employ AMPERE data between 2010–2017, comprising processed magnetic field measurements from the Iridium telecommunications network (Anderson et al., 2000, 2021; Waters et al., 2001, 2020). The dataset is available in files comprising a single day in a single hemisphere, and each file gives Birkeland current densities on a grid of 24 hours of MLT within 50° colatitude of the pole. We adopt the common convention that upward current is positive and downward current is negative. Each grid is available in a sliding window ten minutes long, evaluated every two minutes, such that each day contains 720 timestamps.

In order to conduct the analysis herein, we analyse the AMPERE dataset and find the list of days for which all 720 timestamps are available. This gives 2291 days for our analysis in the Northern Hemisphere and 2324 in the Southern Hemisphere. In this reduced dataset, we iterate through each timestamp and categorise it in one of four categories:

1. Quiet times: not in Walach & Grocott (2019) nor SOPHIE
2. Storm times: in Walach & Grocott (2019) only
3. Quiet-time substorms: in SOPHIE only
4. Storm-time substorms: in both lists

To identify substorms we use SOPHIE (Forsyth et al., 2015), extended to the end of 2017. SOPHIE is defined using percentile thresholds on the rate of change of the SML index called Expansion Phase Thresholds (EPTs); we use an EPT of 75%, which means that a substorm is identified as a negative rate of change in SML above the 75th percentile in each year; in Forsyth et al. (2015) the authors recommend this be used due to similarity with other lists. In addition to the phase descriptions, an "SMU check" flag is set for periods of enhanced convection (when SMU and SML are expected to intensify in tandem) to differentiate them from substorms (where SMU and SML are expected to intensify separately). We count a timestamp as being within a substorm if it is between the start of the substorm expansion phase and the end of the substorm recovery phase as determined by SOPHIE. We do not count timestamps as being within a substorm if they are during expansion/recovery phases for which the SMU check flag is set, nor do we count expansion or recovery phases which do not follow in order; that is to

say, we do not count expansion phases which occur immediately before growth phases and we do not count recovery phases which occur immediately after growth phases.

To identify storms we use the Walach & Grocott (2019) list, extended to the end of 2017. We count a timestamp as being within a storm if it is between the start of the storm initial phase and the end of the storm recovery phase. We define quiet times as any times that have not been categorised as within a storm or substorm according to the above description. We stress that the "quiet times" and "storm times" categories do not contain any substorms.

Lists of the timestamps in each category are presented in the supplementary information, and the numbers of events in each category are as follows. In quiet times, there are 1,119,424 timestamps in the North and 1,134,888 in the South. In storm times, 94,238 and 95,895. In quiet-time substorms, 382,654 and 387,967. In storm-time substorms, 53,204 and 54,530. To make the four categories statistically similar, we subsample randomly to reduce each to 53,000 maps. It is for this reason that we consider data for an eight-year period as opposed to the three-year period used previously (Coxon et al., 2022); this allows our subsamples to be as large as possible. (The subsamples are also presented in the supplementary information.)

3 Mean Birkeland current density per category

Figure 1 shows the mean current density for the four different categories outlined in Section 2 and Figure 2 shows the standard deviation for each of the categories. Figure 1a and 1b show quiet times (non-storm, non-substorm) in the Northern Hemisphere and Southern Hemisphere respectively. The means are weaker in the Southern Hemisphere than in the Northern Hemisphere but the morphology is very similar. The R1 and R2 current systems are clearly visible; the R1 current system lies between $10°-15°$ colatitude on the dayside (at 11 and 13 MLT) and between $16°-21°$ colatitude on the nightside (at 01 and 23 MLT). The R2 current system is equatorward of R1, and slightly thicker; it has a larger latitudinal extent. We interpret the latitudinal extent of each region as a result of averaging over the spatial variation of the current ovals, rather than a sign that the current sheet is getting thicker. There are also current systems poleward of R1 on the dayside which could be NBZ or R0 current systems. Figure 2a–b shows the stan-

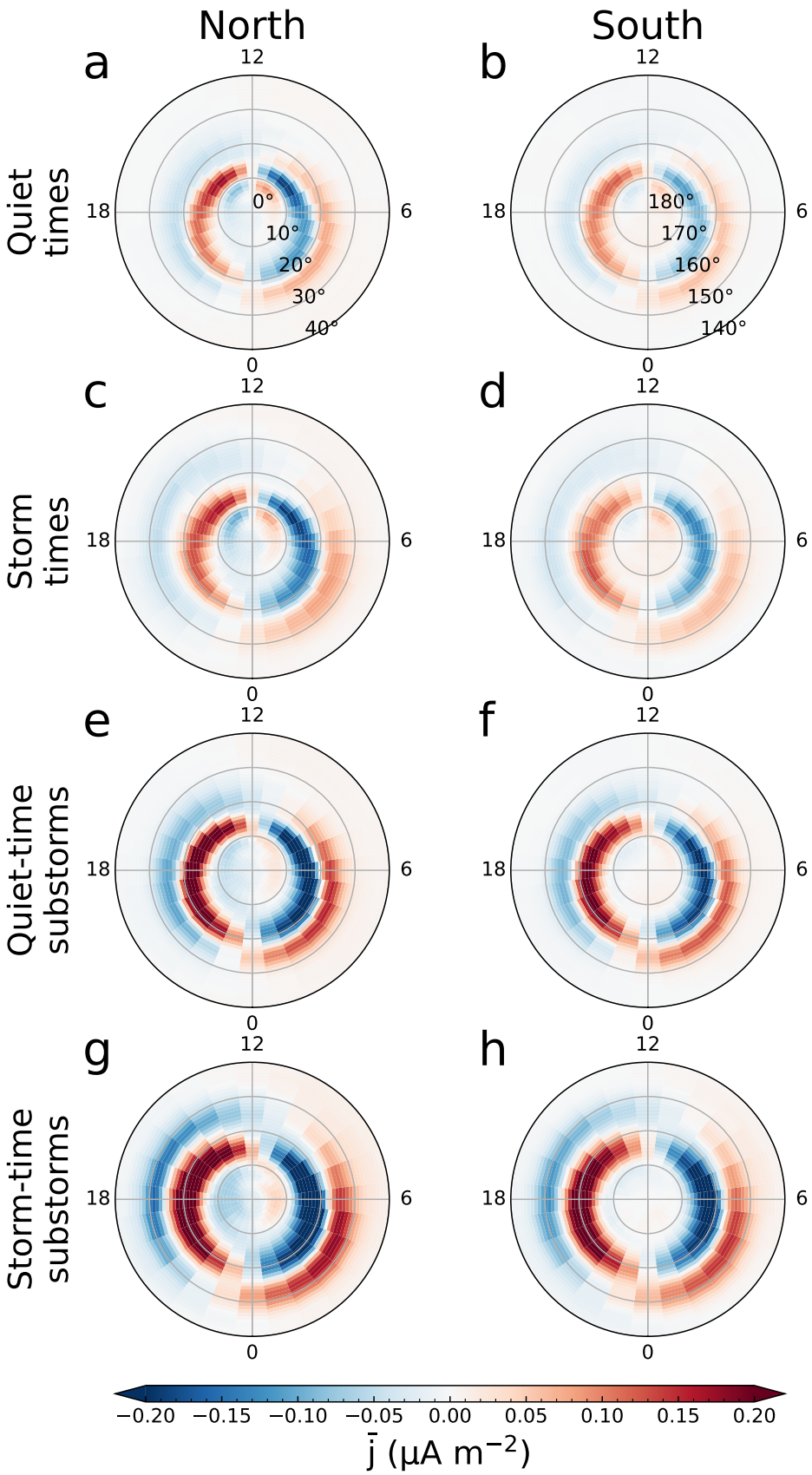

Figure 1. Plots showing the mean current $\bar{j}$ for a–b) quiet times, c–d) storm times, e–f) quiet-time substorms, and g–h) storm-time substorms. The top row is from the Northern Hemisphere and the bottom, the Southern. Numbers around the edges of each plot denote hours of MLT, and each plot shows data $0° - 40°$ from the pole.

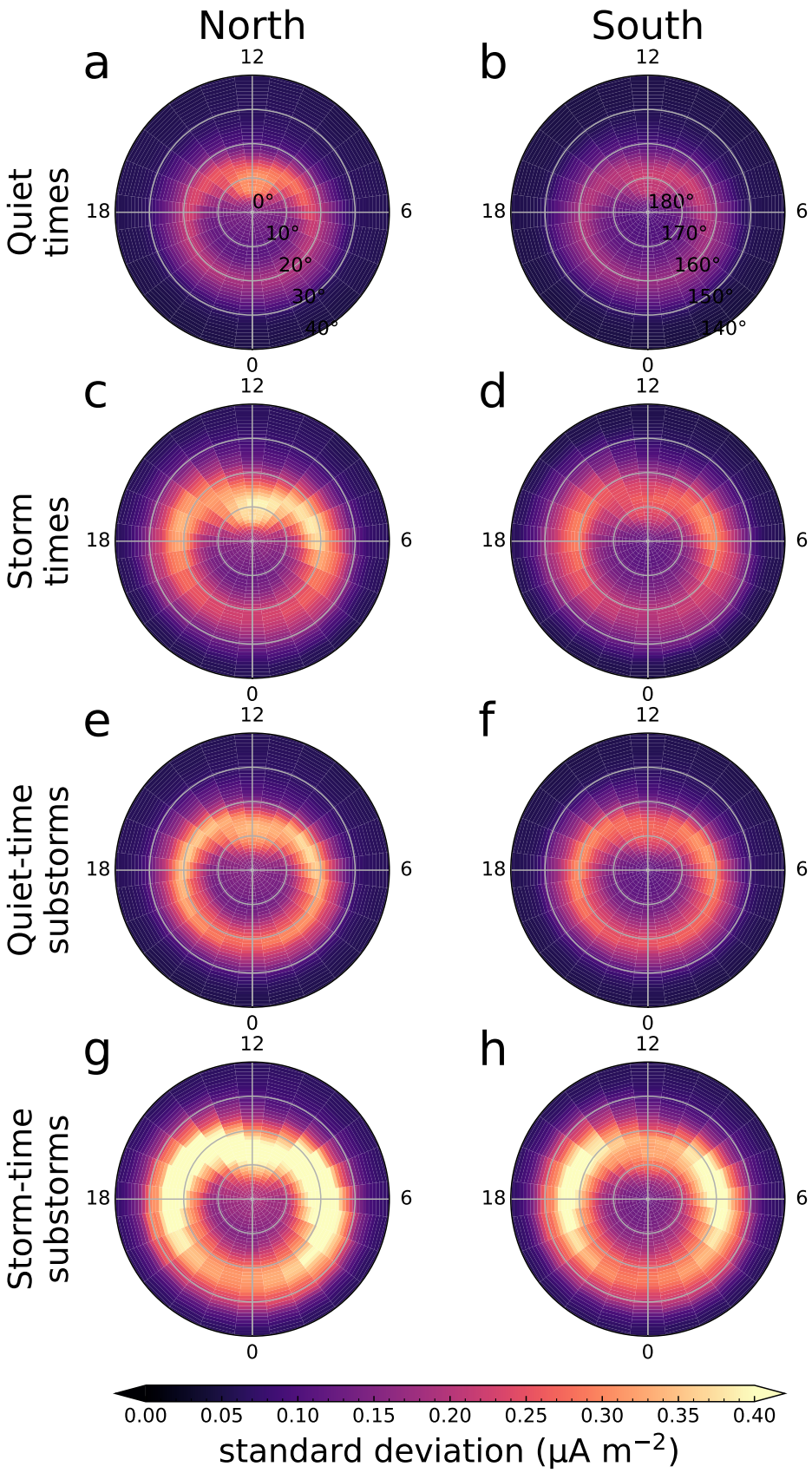

Figure 2. Plots showing the standard deviation in the same format as Figure 1.

dard deviation, which is larger for currents closer to the pole on the dayside (i.e., in the cusp/R0/NBZ current system).

Figure 1c–d show the means for storm times. The regions of non-zero mean current here have a larger latitudinal extent than those for quiet times. The polemost boundary of the R1 current system is the same distance from the pole as in quiet times, but the equatormost boundary is further from the pole. Similar to above, we interpret this increased latitudinal extent as a signature of averaging over a larger range of current oval positions. Since the R1 current oval is located within 1° of the open/closed field line boundary (OCB) (Clausen, Milan, et al., 2013), this implies that geomagnetic storms lead to greater variability of the location of the OCB, and that the OCB reaches lower latitudes during geomagnetic storms than outside these storms. This is consistent with enhanced dayside reconnection combined with the ring current retarding the onset of nightside reconnection (Milan, Grocott, et al., 2009; Milan, Hutchinson, et al., 2009; Milan, 2009). The peak mean current densities are generally similar to quiet times, which may indicate that although the currents vary more spatially they are not, on average, more intense than during quiet times. From the standard deviation of storm times in Figure 2c–d we can see that the variability of the value of current density is higher for storm times than for quiet times across the spatial range observed. As such, although the mean current is very similar, the likelihood of large currents will be higher; this could be because the mean current is being smoothed over a larger area for storms compared to quiet times due to the motion of the OCB. (We address this in more detail in Section 4.)

Figure 1e–f show the means for quiet-time substorms. The mean R1 and R2 current densities during substorms are stronger than they are in the quiet or storm-time categories, whereas the currents poleward of the R1 current system are much weaker. The R1 currents are stronger than the R2 currents, consistent with previous observations (Coxon et al., 2014b, 2017). The R1 current system has a larger latitudinal extent, extending further equatorward than in the previous two categories but with a poleward boundary location which remains the same. Looking at Figure 2e–f, the standard deviations are smaller than for storm times, suggesting that substorms do not lead to variability of current density as high as in storms.

Finally, Figure 1g–h show the means for substorms within storms. The mean current densities are substantially larger than for any other category, and the equatorward

edge of the R1 current system is further from the pole than in any other category. The R2 current system also has a larger latitudinal extent. The mean current density poleward of R1 is approximately the same as for quiet-time substorms. Figure 2g–h shows that the standard deviation in this category is far higher than for the previous three categories.

The means and standard deviations indicate that geomagnetic storms and substorms have different impacts on Birkeland current density, suggesting that substorms lead to higher current on average but that storms are responsible for driving periods of high variability. However, this inference is reliant on describing the underlying distributions by the mean and standard deviation, this occluding a great deal of the underlying variability, especially in the extremes that contribute most to the higher-order moments of the distribution (Coxon et al., 2022). In order to properly quantify the difference between geomagnetic storms and substorms, we proceed to examine the probabilities of low, high, and extreme currents seen during these two events.

4 Probabilities of Birkeland current density per category

We investigate the spatial distributions of different current density thresholds by calculating the probability of current densities above those thresholds in each bin. We refer to these probabilities as $P(J)$ where J is the threshold we set. This method was described fully in Coxon et al. (2022), but briefly recapping it here: we use maximum likelihood estimation to estimate the probability distribution of the underlying data, and then apply the survival function using the probability distribution to recover the probabilities $P(J)$. We fit the probability distribution on either side of the mode current j_m separately, such that we derive the probability distributions for $j > j_m$ and $j < j_m$; for ease of discussion we will refer to these as positive and negative current respectively through the rest of this manuscript.

One update to our method over our previous work is that in cases where Ridders' Method (Ridders, 1979) does not find a solution to the q-exponential fitting, we use a brute force method to explore the parameter space assuming a solution is within the constraints $0.98 \leq q \leq 1.02$ and $0.0 \leq \kappa \leq 0.5$. The former assumption is valid because Ridders' Method only fails to converge when q is close to 1. Therefore, the white "holes" in the maps of the probabilities seen in Coxon et al. (2022) are not reproduced here. We

note that we are modelling the underlying probability distributions, rather than applying probability thresholds to the data directly; this means we can extrapolate to events more extreme than those seen in our interval, but that our selected thresholds do not map to percentiles of the data. We calculate the probability for any appreciable current flow by using a threshold $J = 0.2$ μA m^{-2} in Section 4.1; for high current flow by using a threshold $J = 1.0$ μA m^{-2} in Section 4.2; and for extreme current flow by using a threshold $J = 4.0$ μA m^{-2} in Section 4.3. We select these thresholds to enable comparison to the figures presented in Coxon et al. (2022). We only show plots for the Northern Hemisphere; the corresponding probabilities for the Southern Hemisphere are generally lower, consistent with Coxon et al. (2022), and are presented in the supporting information. We also present bar charts showing the values of the maximum probabilities in each of the maps below (Figures 3–6 and 8–10) in the supporting information as an aid to the reader.

4.1 Probability of low current flowing

Figure 3 shows the probability $P(0.2)$, which is the chance of relatively low current densities (and above); we use this to interpret the probability of appreciable Birkeland current density in a given bin. This minimum threshold also ensures that current densities in each bin are above the 3σ level of the AMPERE dataset (Anderson et al., 2014). Figure 3a–b shows that, for quiet times, the probability is highest (40%) in R1 current on the dayside, and lower for R2 current with no day/nightside dependence. The fact that dayside R1 current is most probable reflects the fact that dayside current reacts to dayside reconnection, and that R1 current reacts to dayside reconnection before the R2 currents (Anderson et al., 2014; Coxon et al., 2019). Currents on the nightside react to nightside reconnection and are therefore more likely to be seen in either of the substorm categories. Figure 3c–d shows that the probability of any current flowing during storm times is very similar to quiet times, but current is more likely to flow further from the pole than it is during quiet times. We interpret this as an indication of the polar cap reaching larger sizes during storms.

Figure 3e–f shows the probability of any current flowing during quiet-time substorms. The probability is highest in R1 at 50% compared to 35% in R2. The spatial extent is similar to that for storm times, but has a larger latitudinal extent on the dayside. In this category, there is no clear difference between dayside and nightside R1 probability whereas

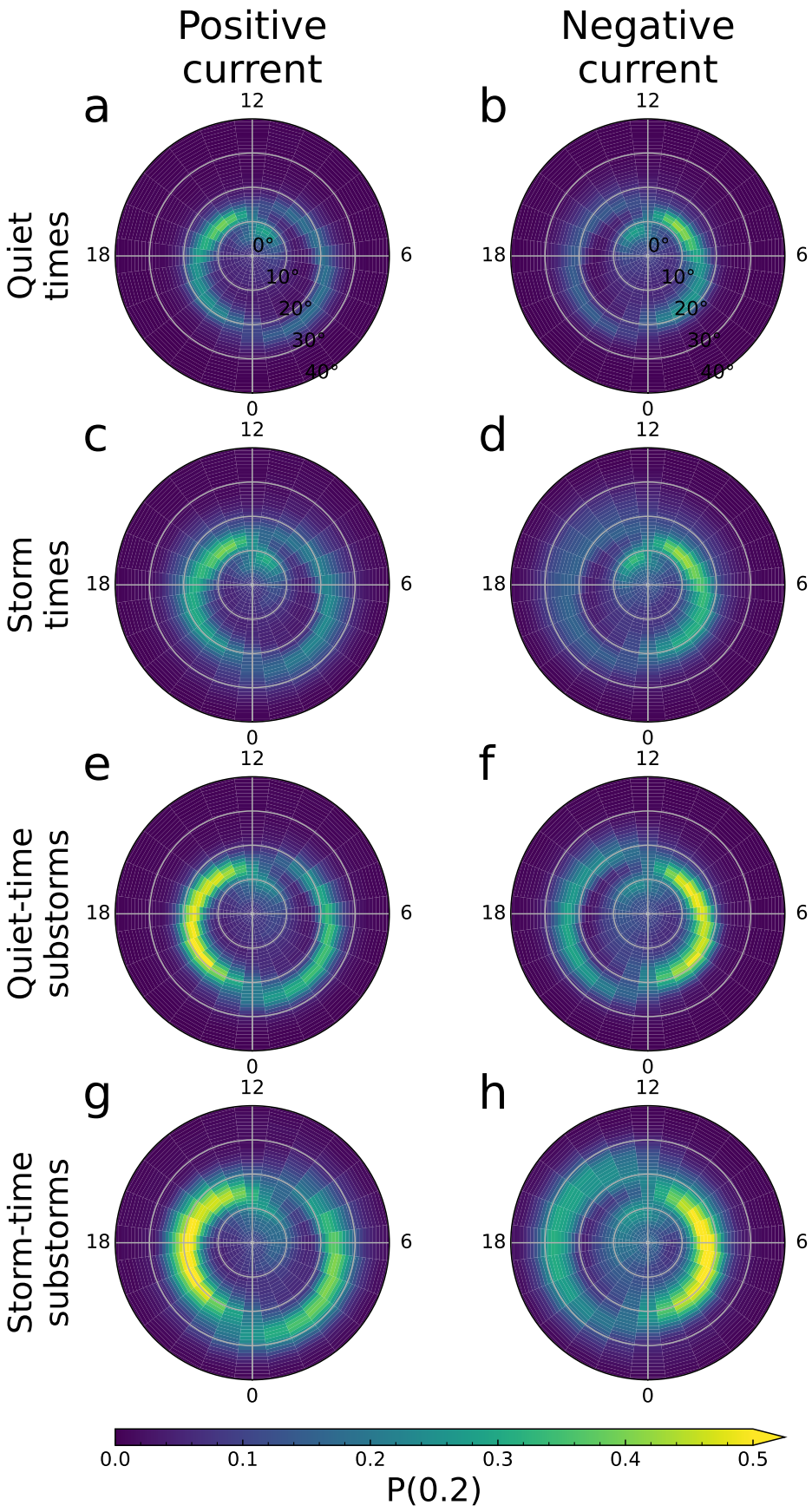

Figure 3. Plots showing $P(0.2)$ for a–b) quiet times, c–d) storm times, e–f) quiet-time substorms, and g–h) storm-time substorms. The top row is for positive current and the bottom row is for negative current.

in R2 the nightside probability is slightly higher. R2 also has higher probabilities in the quiet-time substorms category than in storm times: this is notable because R2 current is thought to close through the partial ring current (Iijima & Potemra, 1978) and storms are associated with elevated ring current, whereas substorms have not explicitly been linked to enhanced ring current other than through storms. If the ring current is typically more enhanced during the main phase of a storm, this observation might be explained by the main phases being shorter than the recovery phases (Hutchinson et al., 2011; Walach & Grocott, 2019). Alternatively, this may simply be because authors have found that R2 current intensifies as part of the substorm current wedge (Anderson et al., 2014, 2018; Coxon et al., 2017; Sergeev, Nikolaev, Tsyganenko, et al., 2014; Sergeev, Nikolaev, Kubyshkina, et al., 2014; Forsyth et al., 2018).

Figure 3g–h shows the probability of any current flowing within storm-time substorms. The probability here reaches 60% for R1 current, and is 40% for R2 in the positive current but only 35% for R2 in the negative current, which appears to be a signature of a dawn-dusk asymmetry. This implies that R1 current is more likely than not to be at appreciable current densities when a substorm occurs within a storm, and that an appreciable R2 current is also likely. Both are more likely than in a substorm outside of a storm.

There is an asymmetry between positive and negative current in each category which we interpret as a dawn-dusk asymmetry; R1 current is more likely for negative current and R2 current is more likely for positive current (the probabilities are more likely on the dusk side). We discuss this in detail in Section 5.2.

4.2 Probability of high current flowing

Figure 4 shows the probability of high current flowing $P(1.0)$. In Coxon et al. (2022) we found that there were two major zones of probability, referred to as Zone A and Zone B (see Figure 5); we adopt the same convention for Figures 4 and 6 in order to avoid making judgements about whether these currents are part of the R1 or R2 current systems. Zone A refers to the more poleward zone of probability, which is on the dusk side for positive current densities and on the dawn side for negative current densities; Zone B refers to the more equatorward region which is on the opposite side to Zone A.

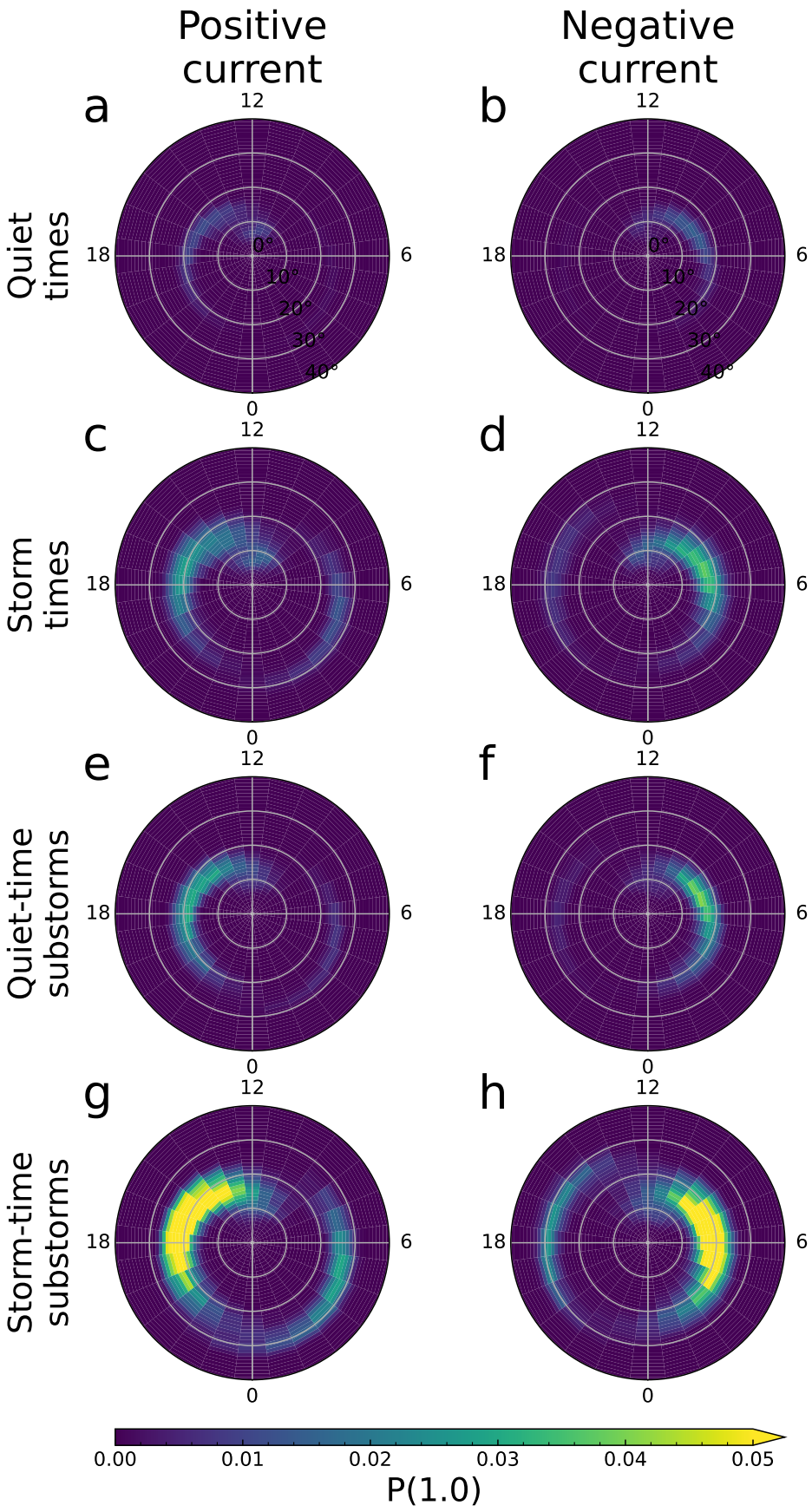

Figure 4. Plots showing $P(1.0)$ in the same format as Figure 3.

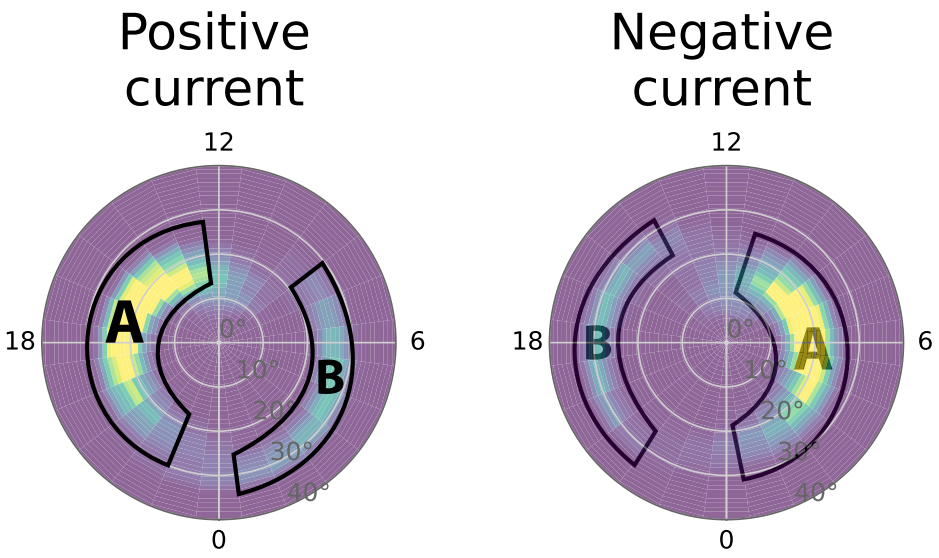

Figure 5. Key to interpreting Zones A and B, used in discussion of Figure 4–10.

The peak probability in Figure 4a–b is approximately 1%, which is far lower than the probability in Figure 3; this is as expected given that we have increased the threshold. In Figure 4a–b, during quiet times, the probability of high current flow is much higher in Zone A than in Zone B (the probability is not zero in Zone B, but it is very low). We note that there is again a dawn-dusk asymmetry. Figure 4c–d shows that the probability of high current is 2–3 times as high in storms as it is for quiet times, and the area of Zone A which is likely to host high current is much wider. Additionally, there is a likelihood of high current in Zone B, which is approximately as likely as in quiet-time Zone A. The difference between panels a–b and c–d in Figure 4 is much larger than the equivalent difference in Figure 3.

Figure 4e–f shows the probability during quiet-time substorms, which has a slightly higher peak in Zone A than for storm times but is more spatially constrained. The probability of current in Zone B is lower than for storm times. Figure 4g–h shows that the probability during storm-time substorms is at least twice as high as in the previous two categories, with the probability in Zone B much stronger and further equatorward than in the previous categories and the spatial range of probability in Zone A much larger than in any previous category. Notably, the probability of current is higher on the dayside than for the nightside in all categories, including substorms.

4.3 Probability of extreme current flowing

Figure 6a–b shows the probability of extreme current flowing $P(4.0)$ during quiet times. The peak likelihood is extremely small (0.04%) in a very small strip in Zone A, with no visible signature in Zone B. The probability of extreme negative current is smaller (0.02%). The probability of extreme current for storm times (Figure 6c–d) is far higher than in quiet times (in contrast to $P(0.2)$ and $P(1.0)$), with the peak 10 times higher and in a much higher spatial extent in Zone A, and a thinner region in Zone B clearly visible at 0.7%.

Notably, the probability of extreme current in quiet-time substorms (Figure 6e) is much more spatially constrained and approximately one third the probability of storm-time extreme currents in Zone A, and has no visible signature in Zone B. As in Figure 4, Figure 6e–f shows that the probability of extreme current is larger on the dayside than on the nightside during quiet-time substorms. For positive current in storm-time substorms (Figure 6g) the peak probability is higher than for storm times in both Zones A and B, and the region of probability is more spatially constrained; however, the difference between storm times and storm-time substorms is not large. Notably, extreme currents are most likely on the dayside and least likely within three hours of midnight, which also allows us to infer that storms are driving these currents.

4.4 Probability integrated over each map

Figure 7 shows the probability $P(J)$ integrated over each map in Figures 3, 4 and 6. We multiply the probability in each cell by the area of that cell, and we sum over all MLT between 0° and 50° colatitude. We divide by the highest integrated value (across the categories and positive/negative current per threshold) to present relative integrals between zero and one. We caution these numbers are in arbitrary units and are only meaningful for comparisons between the maps in this study.

The relative integrated probabilities for $P(0.2)$ (maps in Figure 3) are presented in Figure 7 (left). There is little difference in the relative integral between negative and positive current in any category. The relative integrals for quiet times and for storm-time substorms are as expected from visual inspection of the maps; quiet times have the lowest integral and storm-time substorms have the highest. The integral for storm times is lower than that for the quiet-time substorms; however, the difference is less than a vi-

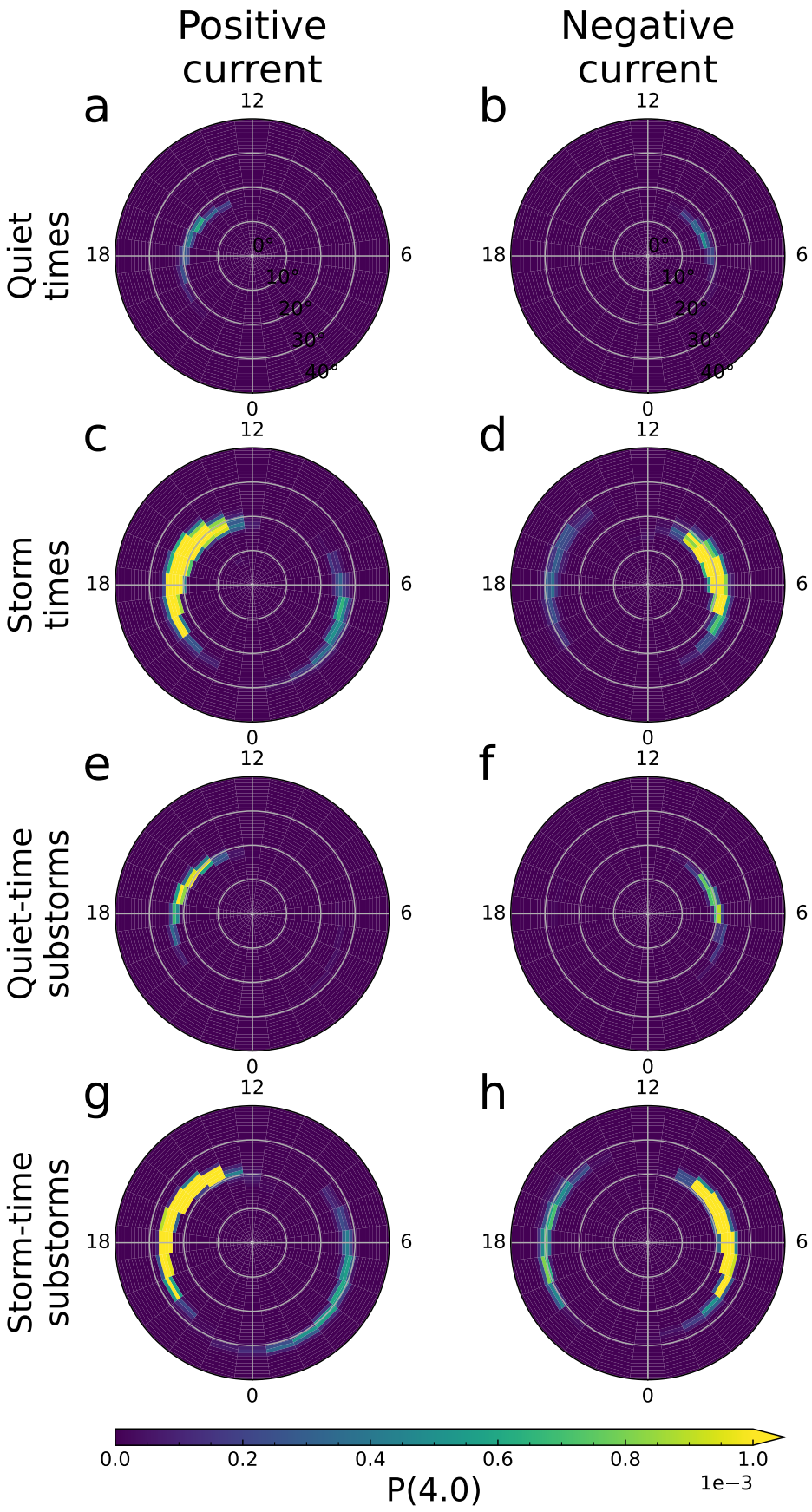

Figure 6. Plots showing $P(4.0)$ in the same format as Figure 3.

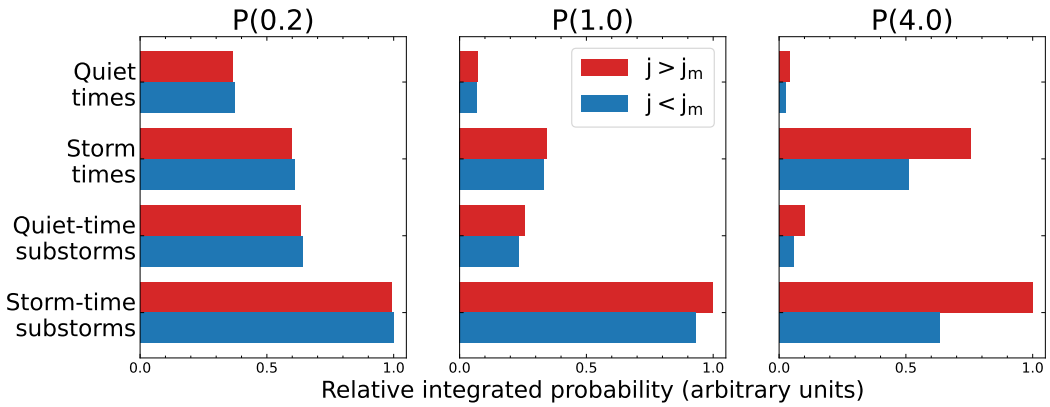

Figure 7. Plots showing the relative integrated probability for each of the maps presented earlier in Section 4. The relative integrals are computed for positive (red) and negative current (blue) for (left) $P(0.2)$, (centre) $P(1.0)$, and (right) $P(4.0)$. For more details, see the text.

sual inspection of Figure 3c–f indicates. This indicates that the spatial smoothing caused by higher variation in current location during geomagnetic storms is reducing the probability in any given bin, but the relative integral is only slightly lower than that for substorms.

Figure 7 (centre) shows the relative integrated probabilities for $P(1.0)$ (maps in Figure 4). Those for quiet times are again lowest, and storm-time substorms are highest. However, in this case, the difference between the relative integrals for quiet times and for storm-time substorms is much larger. The relative integral for storm times is larger than that for quiet-time substorms, contrary to $P(0.2)$. Further, the integrated probability is larger for positive current in all categories, which is the opposite sense to the asymmetry in $P(0.2)$. Figure 7 (right) shows the relative integrals for $P(4.0)$ (maps in Figure 6). This demonstrates the extent to which geomagnetic storms dominate over substorms. The gap between positive and negative current is much wider than at previous thresholds, and the asymmetry is in the same sense as for $P(1.0)$.

4.5 Contributions of R1 and R2 currents

To evaluate the relative contribution of R1 and R2 currents in different categories, we employ an adaptive coordinate system (Chisham, 2017) based on R1-R2 boundaries given in Milan (2019), which are derived from a method outlined in Milan et al. (2015)

and subsequently used to calculate AMPERE proxies for the open/closed field line boundary (Burrell et al., 2020). We refer to these coordinates as Birkeland Current Boundary (BCB) coordinates. In our coordinate system, we iterate through each hour of MLT and shift the current systems in that sector such that the R1-R2 boundary is fixed at a co-latitude of 20°. This means that any currents located poleward of 20° colatitude are R1 currents and any currents located equatorward are R2 currents, by definition. This method was used briefly in Coxon et al. (2022) to try to determine whether the most probable extreme currents were in R1 or in R2.

Figure 8 shows the probability of currents above four thresholds (0.2 μA m^{-2}, 1.0 μA m^{-2}, 2.0 μA m^{-2} and 4.0 μA m^{-2}) for storm times. Panels a–b show the lowest thresholds, and confirm that the regions in Figure 3 map to R1 and R2 current as inferred in Section 4.1. Panels c–d show that Zone A primarily maps to R1 current for $P(1.0)$ and Zone B primarily maps to R2 current. In panel d, the zones are well-separated into R1 and R2, but in panel c the zones are both partly over the 20° colatitude line. This indicates either that the zones are comprised of both R1 and R2 for positive current, or it indicates that the coordinate system is not successfully disentangling R1 and R2 current. For positive current (panels e and g) as the current threshold is raised, Zone A moves equatorward (i.e. the amount of Zone A which is comprised of R1 current decreases) and Zone B moves poleward. For negative current (panels f and h), Zone A becomes less well-defined, shifts towards dawn, and the brighter part moves closer to the pole while Zone B moves slightly equatorward (remaining within R2) and becomes narrower.

Figure 9 shows the probability of currents for quiet-time substorms. $P(0.2)$ (panels a–b) is very similar to the previous figure. For $P(1.0)$ (panels c–d) Zones A and B again primarily map to R1 and R2. Zone A has a larger latitudinal extent in the previous figure than for quiet-time substorms, but stretches further to the nightside here than it does in the previous panel; this is indicative of substorms driving currents on the night side due to nightside reconnection. In comparison to Figure 4, the probability of current on the nightside is higher than it was in AACGM coordinates, which may indicate that plotting the nightside probabilities in AACGM coordinates smooths the probabilities out. However, the probability of strong current is still higher on the dayside than it is on the nightside in BCB coordinates. In panels c–d the probability of Zone B is notably lower than in the storm times (as seen in Figure 4) which is consistent with storms driving more enhanced R2 current than substorms. At higher thresholds (panels e–h)

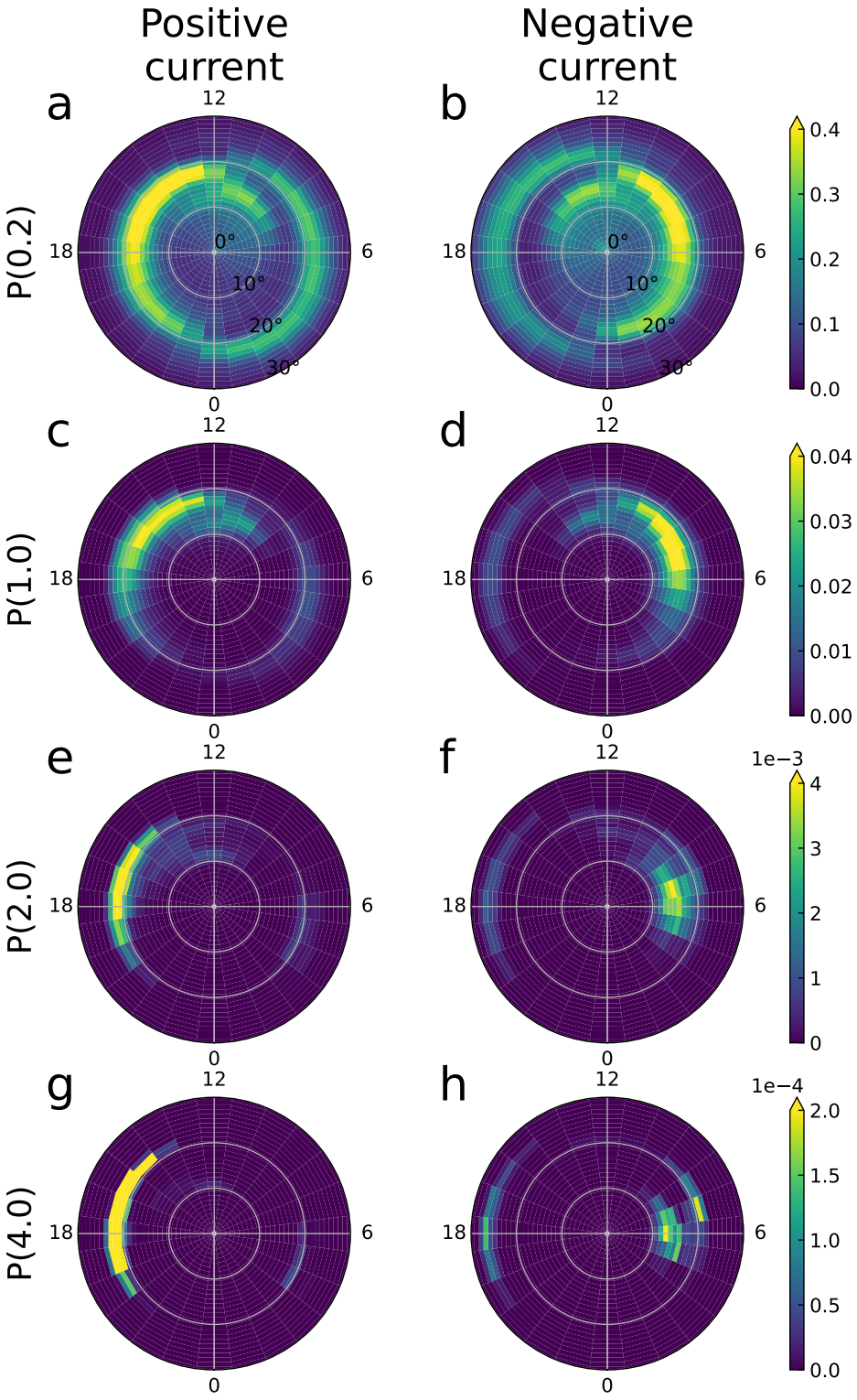

Figure 8. Plots for storm times showing a–b) $P(0.2)$, c–d) $P(1.0)$, e–f) $P(2.0)$, and g–h) $P(4.0)$. The top row is for positive current and the bottom row is for negative current. The parameters are plotted in R1-R2 coordinates (Milan, 2019). Note that the colour scales are different for each column.

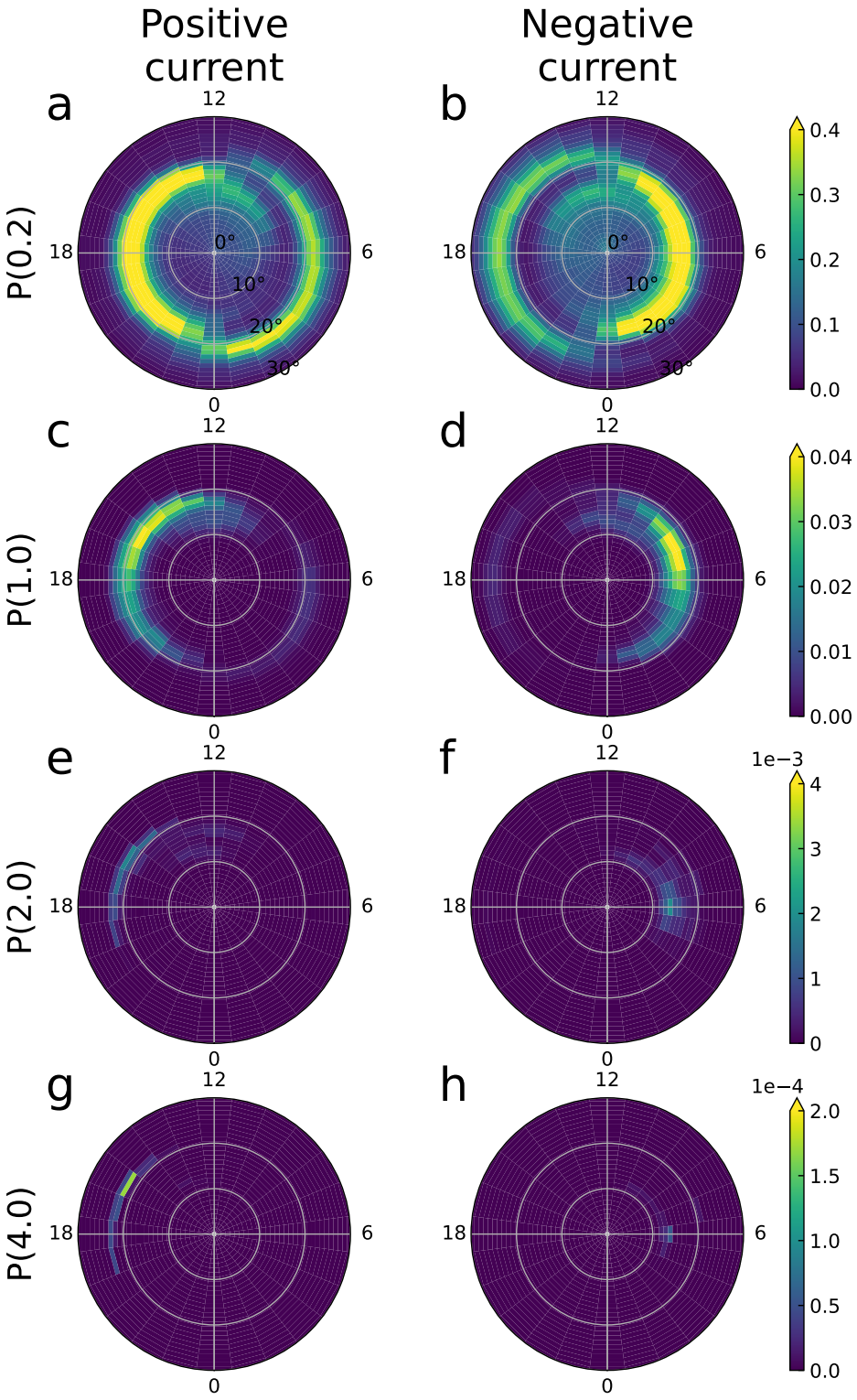

Figure 9. Plots for quiet-time substorms in the same format as Figure 8.

the probabilities are much lower than for storm times and Zone B is invisible on the given colour scale.

Figure 10 shows the probability of currents for storm-time substorms. The morphology of Zones A and B is very similar between Figures 10 and 8 but the probabilities change; in Figure 10a–f the probabilities are higher than in Figure 8, but in panels g–h the probabilities are smaller. This indicates that the most extreme currents are driven during geomagnetic storms during dayside reconnection, and are not driven by nightside reconnection (i.e. substorms) during these periods; this in turn has important ramifications for space weather forecasting and operational awareness.

5 Discussion

To summarise the results presented in Section 4, Figure 1 shows that mean R1 currents are typically larger than mean R2 currents, consistent with our previous work (Coxon et al., 2022) and with previous studies of the large-scale current systems (Anderson et al., 2008; Weimer, 2001). The difference between the means in the four categories is consistent with previous work on substorms, showing that the ratio of R1 to R2 current is larger during substorms than it is outside substorms (Coxon et al., 2014b) and that both current systems intensify during substorms (Coxon et al., 2017). Examination of the current density probabilities between the categories is consistent with the modern view of a storm as a distinct phenomenon (Gonzalez et al., 1994), as we will now discuss.

5.1 The difference between storms and substorms

Our results build a picture in which in which substorms are more likely to drive current in general, but the most extreme currents are much more likely to occur during storms. This is consistent with a view in which storms are characterised by systematically higher variability.

Figure 3 shows that the probability of current density exceeding a low threshold is higher during substorms than it is outside substorms, which indicates that current is more likely to flow during substorm times. This is consistent with Figure 1 showing that mean currents are higher during substorms. The probability of high current is roughly the same in Figure 4c–d as it is in 4e–f, indicating that both storms and substorms lead to higher chance of high current, but is much higher in 4g–h indicating that high cur-

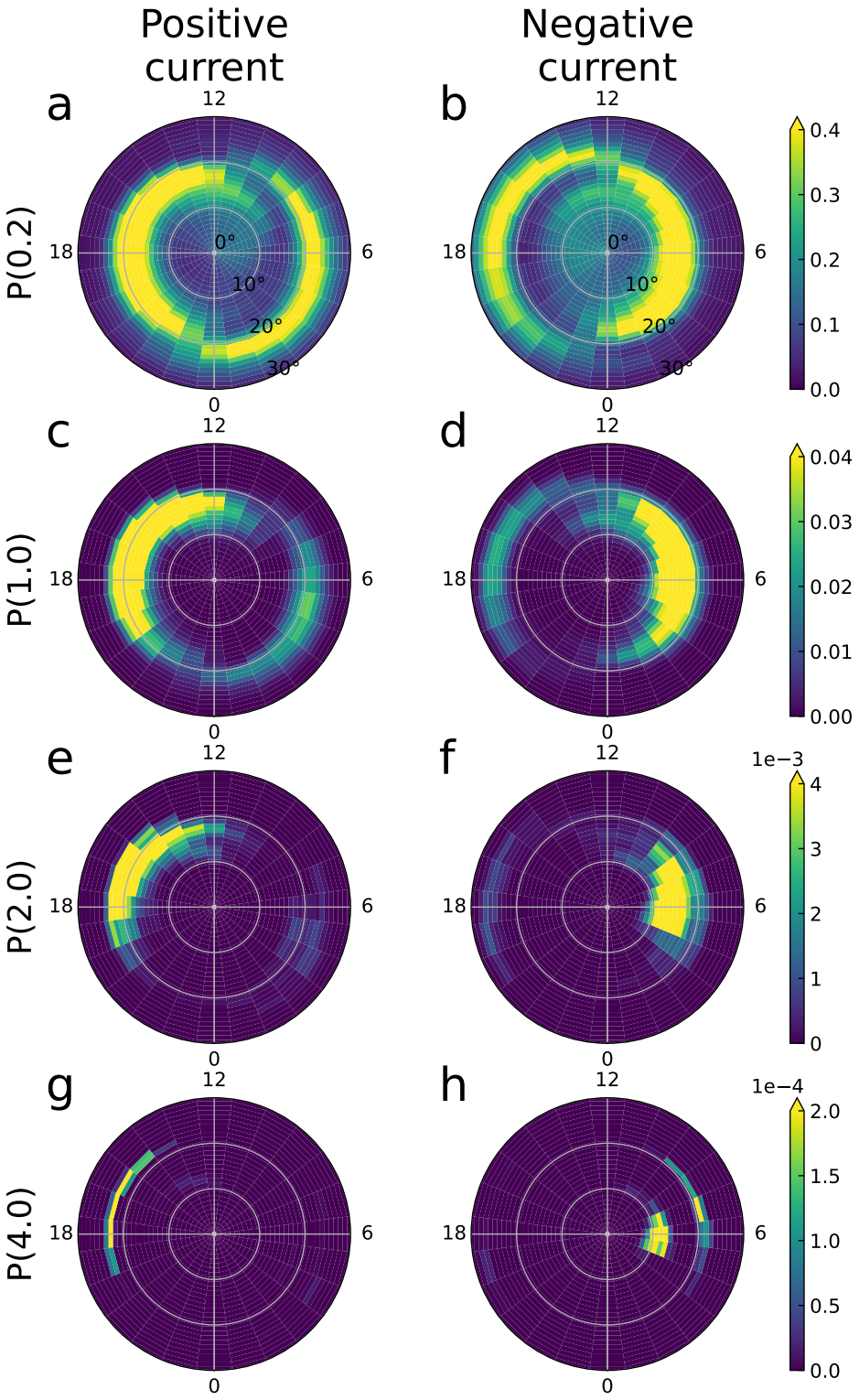

Figure 10. Plots for storm-time substorms in the same format as Figure 8.

rent is most likely in storm-time substorms. Figure 6 shows that the probability of extreme current is much higher during storm times than it is during substorm times, which is consistent with Figure 2.

We find that extreme current densities are most likely on the dayside across all categories, with probabilities highest between 14–20 MLT and 04–10 MLT in storm times and storm-time substorms. This is consistent with the fastest convective flows during geomagnetic storms, which are also largely seen on the dayside (Walach & Grocott, 2019).

These inferences are broadly reinforced by the probabilities plotted in Birkeland Current Boundary (BCB) coordinates, which also demonstrate that current densities exceeding a low threshold are more likely in substorms but that extreme currents are more likely during geomagnetic storms (Figures 8–10). Using BCB coordinates we can attempt to disentangle which current system is responsible for the most extreme currents. We find that the highest probability of extreme current is located within the R2 current system in each of the combinations of substorms and storms examined. Interestingly, in this coordinate system, the highest probability is found during storm times; this may be a sign that the BCB coordinate system is better-ordered by dayside reconnection processes than by substorm processes, and is potentially a note of caution for future work that uses this coordinate system. We also note that the boundary is determined by the current systems seen at dawn and dusk, rather than at noon and midnight where the current systems are less well-defined (Iijima & Potemra, 1978).

Extreme currents are located in the R2 current system. As previously noted in Coxon et al. (2022), this has interesting ramifications. The largest R2 currents flow in the opposite direction to the average R2 current system, which is consistent with previous reports of embedded Birkeland currents (Liu et al., 2021). Physically, we interpret this in the context of enhanced ring current during geomagnetic storms (Chapman & Ferraro, 1933) and the closure of the R2 current system through the ring current (Iijima & Potemra, 1976a, 1978). There is a small region of current $\sim 5^\circ$ poleward of extreme R2 current shown in Figures 8 and 10 and it is not obvious which signature it corresponds to in the AACGM coordinates. However, this may imply that some extreme current is flowing in R1 during storm times, but only on the dawn side flowing into the ionosphere. (We will return to this in the next section.)

In terms of storms and substorms, these results are consistent with work on the rate of change of the surface magnetic field (R). Smith et al. (2019) showed that, in the United Kingdom, more than 90% of the most extreme values of R were observed within three days of a sudden commencement (SC). They further subdivided SCs into sudden impulses (SIs) and storm sudden commencements (SSCs) and showed that the extreme values of R were much more common in SSCs than in SIs, indicating that the extreme behaviour was primarily being observed within geomagnetic storms. Smith et al. (2021) showed that this was also generally true outside of the United Kingdom. Conversely, Freeman et al. (2019) defined extreme values of R as being in the 99.97th percentile, and showed that more than half of these values occurred within substorm expansion and recovery phases, noting that those times only comprised 13.4% of the dataset, concluding that substorms were more likely than generally enhanced convection to display extreme behaviour. They also found that at two of their magnetometers (Hartland and Eskdalemuir) the probability was higher on the dayside, but this was not true for Lerwick. They did not separate substorms according to whether or not they were in geomagnetic storms, however, and it is unclear how their definition of 'extreme' corresponds with ours.

5.2 Dawn-dusk asymmetry in probability

In Figure 3, the probability of R1 current is more likely in the negative current across all categories, and the difference becomes more pronounced from quiet times to storm-time substorms; the R2 current probability is reversed, and R2 current is more likely in the positive current across all categories. This means that the dawn flank shows higher probabilities than on the dusk flank for both current regions. Examination of the corresponding Figure 8 in Coxon et al. (2022) shows the same effect, which was not highlighted in that manuscript. When we increase the thresholds, the extent of the dawn-dusk asymmetry changes: in Figure 4 Zones A and B are higher probability when they are located on the dawn side than when they are on the dusk side but the effect is less obvious. In Figure 6 the opposite is true in all the plots, such that the peak probability in each dusk zone is more pronounced than its dawn counterpart. (For a key to Zones A and B, see Figure 5.)

Examining Figures 8, 9 and 10, we see how this asymmetry manifests in BCB coordinates. Figure 8a–b shows $P(0.2)$ for storm times, and there is no clear dawn-dusk asymmetry in the probabilities. For quiet-time substorms (Figure 9a–b) and storm-time

substorms (Figure 10a–b) both zones A and B show a higher probability on the dawn side than the dusk side for $P(0.2)$, and this is true for all three categories in $P(1.0)$ in BCB coordinates (panels c–d in each figure). Then, for $P(2.0)$ and $P(4.0)$ the effect switches, as it does in AACGM coordinates.

To interpret this asymmetry we first turn to the large-scale morphology shown in Figure 1. This average picture shows that on the dawn side of Earth, R1 current flows downward (into the ionosphere) and R2 current flows upward (out of the ionosphere). The reverse is true on the dusk side. It is thought that the majority of Birkeland current is carried by electrons (Hoffman et al., 1985) and therefore downward currents are associated with electrons travelling up from the ionosphere into the magnetosphere while upward currents are associated with electrons travelling from the magnetosphere into the ionosphere. Cowley (2000) notes that upward currents "are carried by hot magnetospheric electrons moving downwards into the mirror field geometry near the Earth" and that driving sufficient upward current to fulfil the current circuit at Earth requires potential drops to accelerate the electrons down the field lines (Knight, 1973), leading to highly non-linear effects. This may mean that the dawn-dusk asymmetry is caused by the relative abundance of current carriers; it will be easier to carry strong R1 current on the dawn side, owing to the fact that the R1 current is being carried by upward-flowing electrons from the ionosphere on that side. This would explain why the only evidence of extreme R1 current appears to be for downward R1 current flow.

However, on the face of it, this argument seems to be at odds with the fact that R2 currents on the dusk side are also carried by upward-flowing electrons and these currents are also weaker than their dawn counterparts. The relationship between aurora and Birkeland current has been investigated parametrically (Carter et al., 2016), and there is a lack of correspondence on the dusk side between field-aligned currents and the auroral oval, which may lend credence to the idea that this is being driven by some asymmetry in the relationship between current and charge carriers. Conversely, McWilliams et al. (2001) used SuperDARN vorticity to calculate the quantity $J_\parallel/\Sigma_P$ and found that using this method, upward field-aligned current was colocated with aurora from the Polar Visible Imaging System (VIS) in the post-noon sector. Chisham et al. (2007) presented Figure 10c from McWilliams et al. (2001) alongside data from Polar VIS and the Polar Ultraviolet Imager (UVI) in their Figure 11, demonstrating a correspondence between upward current and aurora on both sides of the polar cap. As far as we are aware, these

studies are the only published comparisons between the system-scale positions of field-aligned currents and aurora.

If we turn to a view of the system as a current circuit (e.g. Figure 1 in Cowley, 2000), we can see that on the dawn side the R1 current is flowing into the ionosphere and closing across the polar cap through the R1 current on the dusk side, as well as closing equatorward through the R2 current on the dawn side. This may mean that the strongest current would be expected to be the dawn-side R1 current shortly after both current systems first intensify (Anderson et al., 2014; Coxon et al., 2019). In the large-scale current circuit paradigm, current flowing out through R2 on the dawn side of the ionosphere is expected to close through the partial ring current on the nightside of Earth and back into the ionosphere through R2 on the dusk side (e.g. Ganushkina et al., 2018, and references therein). Any systematic dawn-dusk asymmetry in R2 over a long period of time would require current to flow out through R2 on the dawn side and then not flow back through R2 on the dusk side. This would require current to flow from R2 on the dawn side, through the ring current, and then close through some other current system which was not R2; this may indicate that the current flows are more complex than the large-scale current circuit.

6 Conclusions

The effects of geomagnetic storms and substorms can be differentiated by combining identification methods to identify times at which either or both phenomena are occurring (Forsyth et al., 2015; Walach & Grocott, 2019). We have combined these methods and compared the resulting categories in order to shed light on the ways in which these phenomena affect the probabilities of Birkeland current densities over an eight-year period.

We have shown that geomagnetic storms are characterised by inherently more extreme behaviour, and this means that storms are more likely to drive extreme currents such as those which are most likely to negatively affect operations and infrastructure (Eastwood et al., 2018). This is consistent with previous studies which have shown that the most extreme rates of change of the surface magnetic field are associated with storm sudden commencements (Smith et al., 2021). However, substorms are more likely to drive

appreciable current than storms and consequently the mean currents during substorms are higher than during storms.

In terms of location, we find that extreme currents are more likely on the dayside of Earth than the nightside and least likely within three hours of midnight. We have employed the boundaries between R1 and R2 currents in order to investigate how much each current system contributes to the probability of currents at certain thresholds. We show that the most extreme currents are most likely to flow in the R2 currents on the dusk side in every category.

7 Open Research

The Iridium-derived AMPERE data used in this paper can be obtained from the AMPERE Science Center at https://ampere.jhuapl.edu/. The OMNI data used in this paper can be obtained from NASA/GSFC's Space Physics Data Facility's CDAweb service at https://cdaweb.gsfc.nasa.gov/. The authors would like to thank the AMPERE Science Center and NASA/GSFC for providing data.

R1/R2 Birkeland current radii are available from Milan (2019). SOPHIE phase identifications are available from Forsyth (2023). Storm identifications are available from Walach (2023). Phase identifications are available from Coxon et al. (2023).

Data analysis was conducted in Python 3 using Dask (Rocklin, 2015), matplotlib (Hunter, 2007), NumPy (Harris et al., 2020), SciPy (Virtanen et al., 2020), and SpacePy (Morley et al., 2010).

Acknowledgments

John C Coxon was supported by Science and Technology Facilities Council (STFC) Ernest Rutherford Fellowship ST/V004883/1. Gareth Chisham and Mervyn P Freeman were supported by the British Antarctic Survey (BAS) Polar Science for Planet Earth Programme funded by the Natural Environment Research Council (NERC), and NERC FINESSE grant NE/W003066/1. Colin Forsyth was supported by NERC SWIMMR grant NE/V002724/1. Maria-Theresia Walach was supported by NERC grant NE/T000937/1. Kyle R Murphy was supported by STFC grant ST/V006320/1 and NERC grants NE/P017185/2 and NE/V002554/2. Brian J Anderson and Sarah K Vines were supported by National Science Foundation (NSF) award 2002574. Andrew W Smith was supported by NERC

Independent Research Fellowship NE/W009129/1. Alexandra R Fogg was supported by Irish Research Council Government of Ireland Postdoctoral Fellowship GOIPD/2022/782.

References

Akasofu, S.-I. (1964). The development of the auroral substorm. *Planetary and Space Science*, *12*(4), 273 - 282. Retrieved from http://www.sciencedirect.com/science/article/pii/0032063364901515 doi: https://doi.org/10.1016/0032-0633(64)90151-5

Akasofu, S.-I., Chapman, S., & Venkatesan, D. (1963). The main phase of great magnetic storms. *Journal of Geophysical Research (1896-1977)*, *68*(11), 3345-3350. Retrieved from https://agupubs.onlinelibrary.wiley.com/doi/abs/10.1029/JZ068i011p03345 doi: https://doi.org/10.1029/JZ068i011p03345

Anderson, B. J., Angappan, R., Barik, A., Vines, S. K., Stanley, S., Bernasconi, P. N., ... Barnes, R. J. (2021). Iridium Communications satellite constellation data for study of Earth's magnetic field. *Geochemistry, Geophysics, Geosystems*, *22*(8), e2020GC009515. Retrieved from https://agupubs.onlinelibrary.wiley.com/doi/abs/10.1029/2020GC009515 (e2020GC009515 2020GC009515) doi: https://doi.org/10.1029/2020GC009515

Anderson, B. J., Korth, H., Waters, C. L., Green, D. L., Merkin, V. G., Barnes, R. J., & Dyrud, L. P. (2014). Development of large-scale Birkeland currents determined from the Active Magnetosphere and Planetary Electrodynamics Response Experiment. *Geophysical Research Letters*, *41*(9), 3017–3025. Retrieved from https://doi.org/10.1002/2014GL059941 doi: 10.1002/2014GL059941

Anderson, B. J., Korth, H., Waters, C. L., Green, D. L., & Stauning, P. (2008). Statistical Birkeland current distributions from magnetic field observations by the Iridium constellation. *Annales Geophysicae*, *26*(3), 671–687. Retrieved from http://www.ann-geophys.net/26/671/2008/ doi: 10.5194/angeo-26-671-2008

Anderson, B. J., Olson, C. N., Korth, H., Barnes, R. J., Waters, C. L., & Vines, S. K. (2018). Temporal and spatial development of global Birkeland currents. *Journal of Geophysical Research: Space Physics*, *123*(6), 4785-4808. Retrieved from https://agupubs.onlinelibrary.wiley.com/doi/abs/10.1029/2018JA025254 doi: https://doi.org/10.1029/2018JA025254

Anderson, B. J., Takahashi, K., Kamei, T., Waters, C. L., & Toth, B. A. (2002).

683 Birkeland current system key parameters derived from Iridium observations:
684 Method and initial validation results. *Journal of Geophysical Research: Space*
685 *Physics*, *107*(A6), SMP 11-1–SMP 11-13. Retrieved from https://doi.org/
686 10.1029/2001JA000080 doi: 10.1029/2001JA000080
687 Anderson, B. J., Takahashi, K., & Toth, B. A. (2000). Sensing global Birkeland cur-
688 rents with Iridium engineering magnetometer data. *Geophysical Research Letters*,
689 *27*(24), 4045–4048. Retrieved from https://doi.org/10.1029/2000GL000094
690 doi: 10.1029/2000GL000094
691 Baker, D. N., Pulkkinen, T. I., Angelopoulos, V., Baumjohann, W., & McPherron,
692 R. L. (1996). Neutral line model of substorms: Past results and present view.
693 *Journal of Geophysical Research: Space Physics*, *101*(A6), 12975–13010. Retrieved
694 from https://doi.org/10.1029/95JA03753 doi: 10.1029/95JA03753
695 Billett, D. D., McWilliams, K. A., & Conde, M. G. (2020). Colocated observa-
696 tions of the E and F region thermosphere during a substorm. *Journal of Geo-*
697 *physical Research: Space Physics*, *125*(11), e2020JA028165. Retrieved from
698 https://agupubs.onlinelibrary.wiley.com/doi/abs/10.1029/2020JA028165
699 (e2020JA028165 10.1029/2020JA028165) doi: https://doi.org/10.1029/
700 2020JA028165
701 Birkeland, K. (1908). (Vol. 1). Christiania, Norway: H. Aschelhoug & Co.
702 Birkeland, K. (1913). (Vol. 2). Christiania, Norway: H. Aschelhoug & Co.
703 Burrell, A. G., Chisham, G., Milan, S. E., Kilcommons, L., Chen, Y.-J., Thomas,
704 E. G., & Anderson, B. (2020). AMPERE polar cap boundaries. *Annales Geo-*
705 *physicae*, *38*(2), 481–490. Retrieved from https://angeo.copernicus.org/
706 articles/38/481/2020/ doi: 10.5194/angeo-38-481-2020
707 Burton, R. K., McPherron, R. L., & Russell, C. T. (1975). An empirical relation-
708 ship between interplanetary conditions and D_{st}. *Journal of Geophysical Research*,
709 *80*(31), 4204–4214. Retrieved from https://doi.org/10.1029/JA080i031p04204
710 doi: 10.1029/JA080i031p04204
711 Carter, J. A., Milan, S. E., Coxon, J. C., Walach, M.-T., & Anderson, B. J. (2016).
712 Average field-aligned current configuration parameterized by solar wind con-
713 ditions. *Journal of Geophysical Research: Space Physics*. Retrieved from
714 https://doi.org/10.1002/2015JA021567 doi: 10.1002/2015JA021567
715 Chapman, S., & Bartels, J. (1940). *Geomagnetism*. Oxford, UK: Clarendon Press.

Retrieved from https://books.google.co.uk/books?id=_NQgAAAAMAAJ

Chapman, S., & Ferraro, V. C. A. (1931). A new theory of magnetic storms. *Terrestrial Magnetism and Atmospheric Electricity*, *36*(2), 77–97. Retrieved from https://doi.org/10.1029/TE036i002p00077 doi: 10.1029/TE036i002p00077

Chapman, S., & Ferraro, V. C. A. (1933). A new theory of magnetic storms. *Terrestrial Magnetism and Atmospheric Electricity*, *38*(2), 79–96. Retrieved from https://doi.org/10.1029/TE038i002p00079 doi: 10.1029/TE038i002p00079

Chisham, G. (2017). A new methodology for the development of high-latitude ionospheric climatologies and empirical models. *Journal of Geophysical Research: Space Physics*, *122*(1), 932-947. Retrieved from https://agupubs.onlinelibrary.wiley.com/doi/abs/10.1002/2016JA023235 doi: https://doi.org/10.1002/2016JA023235

Chisham, G., & Freeman, M. P. (2010). On the non-Gaussian nature of ionospheric vorticity. *Geophysical Research Letters*, *37*(12). Retrieved from https://agupubs.onlinelibrary.wiley.com/doi/abs/10.1029/2010GL043714 doi: 10.1029/2010GL043714

Chisham, G., & Freeman, M. P. (2021). A statistical model of vorticity in the polar ionosphere and implications for extreme values. *Journal of Geophysical Research: Space Physics*, *126*(11), e2021JA029307. Retrieved from https://agupubs.onlinelibrary.wiley.com/doi/abs/10.1029/2021JA029307 (e2021JA029307 2021JA029307) doi: https://doi.org/10.1029/2021JA029307

Chisham, G., Freeman, M. P., Abel, G. A., Bristow, W. A., Marchaudon, A., Ruohoniemi, J. M., & Sofko, G. J. (2009). Spatial distribution of average vorticity in the high-latitude ionosphere and its variation with interplanetary magnetic field direction and season. *Journal of Geophysical Research: Space Physics*, *114*(A9). Retrieved from https://doi.org/10.1029/2009JA014263 doi: 10.1029/2009JA014263

Chisham, G., Lester, M., Milan, S. E., Freeman, M. P., Bristow, W. A., Grocott, A., ... Walker, A. D. M. (2007, Jan 01). A decade of the Super Dual Auroral Radar Network (SuperDARN): scientific achievements, new techniques and future directions. *Surveys in Geophysics*, *28*(1), 33-109. Retrieved from https://doi.org/10.1007/s10712-007-9017-8 doi: 10.1007/s10712-007-9017-8

Clausen, L. B. N., Baker, J. B. H., Ruohoniemi, J. M., Milan, S. E., Coxon, J. C.,

Wing, S., ... Anderson, B. J. (2013). Temporal and spatial dynamics of the regions 1 and 2 Birkeland currents during substorms. *Journal of Geophysical Research: Space Physics*, *118*(6), 3007–3016. doi: 10.1002/jgra.50288

Clausen, L. B. N., Milan, S. E., Baker, J. B. H., Ruohoniemi, J. M., Glassmeier, K.-H., Coxon, J. C., & Anderson, B. J. (2013). On the influence of open magnetic flux on substorm intensity: Ground- and space-based observations. *Journal of Geophysical Research: Space Physics*, *118*(6), 2958–2969. doi: 10.1002/jgra.50308

Cowley, S. W. H. (2000). Magnetosphere-ionosphere interactions: A tutorial review. In S.-I. Ohtani, R. Fujii, M. Hesse, & R. L. Lysak (Eds.), *Magnetospheric current systems* (Vol. 118, pp. 91–106). Washington, DC, USA: American Geophysical Union. Retrieved from `http://www.agu.org/books/gm/v118/GM118p0091/GM118p0091.shtml`

Cowley, S. W. H., & Lockwood, M. (1992). Excitation and decay of solar wind-driven flows in the magnetosphere-ionosphere system. *Annales Geophysicae*, *10*, 103–115.

Coxon, J. C., Chisham, G., Freeman, M. P., Anderson, B. J., & Fear, R. C. (2022). Distributions of Birkeland current density observed by AMPERE are heavy-tailed or long-tailed. *Journal of Geophysical Research: Space Physics*, *127*(2), e2021JA029801. Retrieved from `https://agupubs.onlinelibrary.wiley.com/doi/abs/10.1029/2021JA029801` (e2021JA029801 2021JA029801) doi: https://doi.org/10.1029/2021JA029801

Coxon, J. C., Forsyth, C., & Walach, M.-T. (2023). *Unique categories of geomagnetic activity 2010–2017* [Dataset]. Northumbria University. Retrieved from `https://figshare.northumbria.ac.uk/account/items/24420817/` doi: 10.25398/rd.northumbria.24420817

Coxon, J. C., Freeman, M. P., Jackman, C. M., Forsyth, C., Rae, I. J., & Fear, R. C. (2018). Tailward propagation of magnetic energy density variations with respect to substorm onset times. *Journal of Geophysical Research: Space Physics*. Retrieved from `https://agupubs.onlinelibrary.wiley.com/doi/abs/10.1029/2017JA025147` doi: 10.1029/2017JA025147

Coxon, J. C., Milan, S. E., & Anderson, B. J. (2018). A review of Birkeland current research using AMPERE. In A. Keiling, O. Marghitu, & M. Wheatland (Eds.),

Electric currents in geospace and beyond (p. 257-278). American Geophysical Union (AGU). Retrieved from https://agupubs.onlinelibrary.wiley.com/doi/abs/10.1002/9781119324522.ch16 doi: 10.1002/9781119324522.ch16

Coxon, J. C., Milan, S. E., Carter, J. A., Clausen, L. B. N., Anderson, B. J., & Korth, H. (2016). Seasonal and diurnal variations in AMPERE observations of the Birkeland currents compared to modeled results. *Journal of Geophysical Research: Space Physics*, *121*(5), 4027–4040. Retrieved from https://doi.org/10.1002/2015JA022050 doi: 10.1002/2015JA022050

Coxon, J. C., Milan, S. E., Clausen, L. B. N., Anderson, B. J., & Korth, H. (2014a). The magnitudes of the regions 1 and 2 Birkeland currents observed by AMPERE and their role in solar wind-magnetosphere-ionosphere coupling. *Journal of Geophysical Research: Space Physics*, *119*(12), 9804–9815. Retrieved from https://doi.org/10.1002/2014JA020138 doi: 10.1002/2014JA020138

Coxon, J. C., Milan, S. E., Clausen, L. B. N., Anderson, B. J., & Korth, H. (2014b). A superposed epoch analysis of the regions 1 and 2 Birkeland currents observed by AMPERE during substorms. *Journal of Geophysical Research: Space Physics*, *119*(12), 9834–9846. Retrieved from https://doi.org/10.1002/2014JA020500 doi: 10.1002/2014JA020500

Coxon, J. C., Rae, I. J., Forsyth, C., Jackman, C. M., Fear, R. C., & Anderson, B. J. (2017). Birkeland currents during substorms: Statistical evidence for a Region 2 intensification after onset and a local reduction in density before onset. *Journal of Geophysical Research: Space Physics*. Retrieved from https://doi.org/10.1002/2017JA023967 doi: 10.1002/2017JA023967

Coxon, J. C., Shore, R. M., Freeman, M. P., Fear, R. C., Browett, S. D., Smith, A. W., ... Anderson, B. J. (2019). Timescales of Birkeland currents driven by the IMF. *Geophysical Research Letters*, *46*(14), 7893-7901. Retrieved from https://agupubs.onlinelibrary.wiley.com/doi/abs/10.1029/2018GL081658 doi: 10.1029/2018GL081658

Dungey, J. W. (1961). Interplanetary magnetic field and the auroral zones. *Physics Review Letters*, *6*, 47–48.

Eastwood, J. P., Hapgood, M. A., Biffis, E., Benedetti, D., Bisi, M. M., Green, L., ... Burnett, C. (2018). Quantifying the economic value of space weather forecasting for power grids: An exploratory study. *Space Weather*, *16*(12), 2052-2067.

Retrieved from https://agupubs.onlinelibrary.wiley.com/doi/abs/10.1029/2018SW002003 doi: 10.1029/2018SW002003

Ebihara, Y., & Tanaka, T. (2023). Generation of field-aligned currents during substorm expansion: An update. *Journal of Geophysical Research: Space Physics*, *128*(2), e2022JA031011. Retrieved from https://agupubs.onlinelibrary.wiley.com/doi/abs/10.1029/2022JA031011 doi: https://doi.org/10.1029/2022JA031011

Forsyth, C. (2023, 11). *Substorm onsets and phases (SOPHIE) 2010-2020, EPT 75* [Dataset]. University College London. Retrieved from https://rdr.ucl.ac.uk/articles/dataset/Substorm_Onsets_and_Phases_SOPHIE_2010-2020_EPT_75/24321142 doi: 10.5522/04/24321142.v1

Forsyth, C., Fazakerley, A. N., Rae, I. J., J. Watt, C. E., Murphy, K., Wild, J. A., ... Zhang, Y. (2014). In situ spatiotemporal measurements of the detailed azimuthal substructure of the substorm current wedge. *Journal of Geophysical Research: Space Physics*, *119*(2), 927–946. Retrieved from https://doi.org/10.1002/2013JA019302 doi: 10.1002/2013JA019302

Forsyth, C., Rae, I. J., Coxon, J. C., Freeman, M. P., Jackman, C. M., Gjerloev, J., & Fazakerley, A. N. (2015). A new technique for determining Substorm Onsets and Phases from Indices of the Electrojet (SOPHIE). *Journal of Geophysical Research: Space Physics*, *120*(12), 10,592–10,606. Retrieved from https://doi.org/10.1002/2015JA021343 doi: 10.1002/2015JA021343

Forsyth, C., Rae, I. J., Murphy, K. R., Freeman, M. P., Huang, C.-L., Spence, H. E., ... Watt, C. E. J. (2016). What effect do substorms have on the content of the radiation belts? *Journal of Geophysical Research: Space Physics*, *121*(7), 6292–6306. Retrieved from https://doi.org/10.1002/2016JA022620 doi: 10.1002/2016JA022620

Forsyth, C., Shortt, M., Coxon, J. C., Rae, I. J., Freeman, M. P., Kalmoni, N. M. E., ... Burrell, A. G. (2018). Seasonal and temporal variations of field-aligned currents and ground magnetic deflections during substorms. *Journal of Geophysical Research: Space Physics*, *123*(4), 2696-2713. Retrieved from https://agupubs.onlinelibrary.wiley.com/doi/abs/10.1002/2017JA025136 doi: https://doi.org/10.1002/2017JA025136

Freeman, M. P., Forsyth, C., & Rae, I. J. (2019). The influence of sub-

storms on extreme rates of change of the surface horizontal magnetic field in the United Kingdom. *Space Weather*, *17*(6), 827-844. Retrieved from https://agupubs.onlinelibrary.wiley.com/doi/abs/10.1029/2018SW002148 doi: 10.1029/2018SW002148

Freeman, M. P., & Morley, S. K. (2009). No evidence for externally triggered substorms based on superposed epoch analysis of IMF B_z. *Geophysical Research Letters*, *36*(21). Retrieved from https://doi.org/10.1029/2009GL040621 doi: 10.1029/2009GL040621

Frey, H. U., Mende, S. B., Angelopoulos, V., & Donovan, E. F. (2004). Substorm onset observations by IMAGE-FUV. *Journal of Geophysical Research: Space Physics*, *109*(A10). Retrieved from https://doi.org/10.1029/2004JA010607 (A10304) doi: 10.1029/2004JA010607

Ganushkina, N. Y., Liemohn, M. W., & Dubyagin, S. (2018). Current systems in the Earth's magnetosphere. *Reviews of Geophysics*, *56*(2), 309-332. Retrieved from https://agupubs.onlinelibrary.wiley.com/doi/abs/10.1002/2017RG000590 doi: https://doi.org/10.1002/2017RG000590

Gonzalez, W. D., Joselyn, J. A., Kamide, Y., Kroehl, H. W., Rostoker, G., Tsurutani, B. T., & Vasyliunas, V. M. (1994). What is a geomagnetic storm? *Journal of Geophysical Research: Space Physics*, *99*(A4), 5771-5792. Retrieved from https://agupubs.onlinelibrary.wiley.com/doi/abs/10.1029/93JA02867 doi: https://doi.org/10.1029/93JA02867

Gonzalez, W. D., & Tsurutani, B. T. (1987). Criteria of interplanetary parameters causing intense magnetic storms (Dst $<$ -100 nT). *Planetary and Space Science*, *35*(9), 1101-1109. Retrieved from https://www.sciencedirect.com/science/article/pii/0032063387900158 doi: https://doi.org/10.1016/0032-0633(87)90015-8

Harris, C. R., Millman, K. J., van der Walt, S. J., Gommers, R., Virtanen, P., Cournapeau, D., ... Oliphant, T. E. (2020, Sep 01). Array programming with NumPy. *Nature*, *585*(7825), 357–362. Retrieved from https://doi.org/10.1038/s41586-020-2649-2 doi: 10.1038/s41586-020-2649-2

Hoffman, R., Sugiura, M., & Maynard, N. (1985). Current carriers for the field-aligned current system. *Advances in Space Research*, *5*(4), 109-126. Retrieved from https://www.sciencedirect.com/science/article/pii/

0273117785901243 doi: https://doi.org/10.1016/0273-1177(85)90124-3

Hunter, J. D. (2007). Matplotlib: A 2D graphics environment. *Computing in Science & Engineering*, *9*(3), 90-95. Retrieved from http://aip.scitation.org/doi/abs/10.1109/MCSE.2007.55 doi: 10.1109/MCSE.2007.55

Hutchinson, J. A., Wright, D. M., & Milan, S. E. (2011). Geomagnetic storms over the last solar cycle: A superposed epoch analysis. *Journal of Geophysical Research: Space Physics*, *116*(A9). Retrieved from https://agupubs.onlinelibrary.wiley.com/doi/abs/10.1029/2011JA016463 doi: https://doi.org/19.1029/2011JA016463

Iijima, T., & Potemra, T. A. (1976a). The amplitude distribution of field-aligned currents at northern high latitudes observed by Triad. *Journal of Geophysical Research*, *81*, 2165–2174.

Iijima, T., & Potemra, T. A. (1976b). Field-aligned currents in the dayside cusp observed by Triad. *Journal of Geophysical Research*, *81*, 5971–5979.

Iijima, T., & Potemra, T. A. (1978). Large-scale characteristics of field-aligned currents associated with substorms. *Journal of Geophysical Research: Space Physics*, *83*(A2), 599-615. Retrieved from https://agupubs.onlinelibrary.wiley.com/doi/abs/10.1029/JA083iA02p00599 doi: 10.1029/JA083iA02p00599

Iijima, T., Potemra, T. A., Zanetti, L. J., & Bythrow, P. F. (1984). Large-scale Birkeland currents in the dayside polar region during strongly northward IMF: A new Birkeland current system. *Journal of Geophysical Research: Space Physics*, *89*(A9), 7441–7452. Retrieved from https://doi.org/10.1029/JA089iA09p07441 doi: 10.1029/JA089iA09p07441

Imajo, S., Nosé, M., Aida, M., Higashio, N., Matsumoto, H., Kiyokazu, K., ... Yoshikawa, A. (2020, May 07). Evolution of field-aligned current in the meridional plane during substorm: multipoint observations from satellites and ground stations. *Earth, Planets and Space*, *72*(1), 58. Retrieved from https://doi.org/10.1186/s40623-020-01182-6 doi: 10.1186/s40623-020-01182-6

Kleimenova, N. G., Gromova, L. I., Gromov, S. V., & Malysheva, L. M. (2021, Jul 01). High-latitude geomagnetic disturbances and field aligned currents in the recovery phase of the large magnetic storm on June 21–26, 2015. *Geomagnetism and Aeronomy*, *61*(4), 520–530. Retrieved from https://doi.org/10.1134/S0016793221040071 doi: 10.1134/S0016793221040071

Knight, S. (1973). Parallel electric fields. *Planetary and Space Science*, *21*(5), 741 - 750. Retrieved from http://www.sciencedirect.com/science/article/pii/0032063373900937 doi: https://doi.org/10.1016/0032-0633(73)90093-7

Kokubun, S. (1972). Relationship of interplanetary magnetic field structure with development of substorm and storm main phase. *Planetary and Space Science*, *20*(7), 1033-1049. Retrieved from https://www.sciencedirect.com/science/article/pii/0032063372902140 doi: https://doi.org/10.1016/0032-0633(72)90214-0

Kunduri, B. S. R., Maimaiti, M., Baker, J. B. H., Ruohoniemi, J. M., Anderson, B. J., & Vines, S. K. (2020). A deep learning-based approach for modeling the dynamics of AMPERE Birkeland currents. *Journal of Geophysical Research: Space Physics*, *125*(8), e2020JA027908. Retrieved from https://agupubs.onlinelibrary.wiley.com/doi/abs/10.1029/2020JA027908 (e2020JA027908 10.1029/2020JA027908) doi: https://doi.org/10.1029/2020JA027908

Laundal, K. M., Cnossen, I., Milan, S. E., Haaland, S. E., Coxon, J., Pedatella, N. M., ... Reistad, J. P. (2017). North–south asymmetries in Earth's magnetic field. *Space Science Reviews*, *206*(1), 225–257. Retrieved from https://doi.org/10.1007/s11214-016-0273-0 doi: 10.1007/s11214-016-0273-0

Liu, J., Lyons, L. R., Wang, C.-P., Ma, Y., Strangeway, R. J., Zhang, Y., ... Khurana, K. (2021). Embedded Regions 1 and 2 field-aligned currents: Newly recognized from low-altitude spacecraft observations. *Journal of Geophysical Research: Space Physics*, *126*(6), e2021JA029207. Retrieved from https://agupubs.onlinelibrary.wiley.com/doi/abs/10.1029/2021JA029207 (e2021JA029207 2021JA029207) doi: https://doi.org/10.1029/2021JA029207

Loewe, C. A., & Prölss, G. W. (1997). Classification and mean behavior of magnetic storms. *Journal of Geophysical Research: Space Physics*, *102*(A7), 14209-14213. Retrieved from https://agupubs.onlinelibrary.wiley.com/doi/abs/10.1029/96JA04020 doi: https://doi.org/10.1029/96JA04020

Lukianova, R. Y. (2020a, Mar 01). Extreme field-aligned currents during magnetic storms of the 24th solar cycle: March 2015 and September 2017. *Cosmic Research*, *58*(2), 65–78. Retrieved from https://doi.org/10.1134/S0010952520020069 doi: 10.1134/S0010952520020069

Lukianova, R. Y. (2020b). Swarm field-aligned currents during a severe magnetic

storm of September 2017. *Annales Geophysicae*, *38*(1), 191–206. Retrieved from https://angeo.copernicus.org/articles/38/191/2020/ doi: 10.5194/angeo-38-191-2020

Maute, A., Richmond, A. D., Lu, G., Knipp, D. J., Shi, Y., & Anderson, B. (2021). Magnetosphere-ionosphere coupling via prescribed field-aligned current simulated by the TIEGCM. *Journal of Geophysical Research: Space Physics*, *126*(1), e2020JA028665. Retrieved from https://agupubs.onlinelibrary.wiley.com/doi/abs/10.1029/2020JA028665 (e2020JA028665 2020JA028665) doi: https://doi.org/10.1029/2020JA028665

McPherron, R. L. (1970). Growth phase of magnetospheric substorms. *Journal of Geophysical Research*, *75*(28), 5592–5599. Retrieved from https://doi.org/10.1029/JA075i028p05592 doi: 10.1029/JA075i028p05592

McWilliams, K. A., Yeoman, T. K., Sigwarth, J. B., Frank, L. A., & Brittnacher, M. (2001). The dayside ultraviolet aurora and convection responses to a southward turning of the interplanetary magnetic field. *Annales Geophysicae*, *19*(7), 707–721. Retrieved from http://www.ann-geophys.net/19/707/2001/ doi: 10.5194/angeo-19-707-2001

Milan, S. E. (2009). Both solar wind-magnetosphere coupling and ring current intensity control of the size of the auroral oval. *Geophysical Research Letters*, *36*(18). doi: 10.1029/2009GL039997

Milan, S. E. (2019, 12). *AMPERE R1/R2 FAC radii* [Dataset]. Retrieved from https://leicester.figshare.com/articles/dataset/AMPERE_R1_R2_FAC_radii/11294861 doi: 10.25392/leicester.data.11294861.v1

Milan, S. E., Carter, J. A., Korth, H., & Anderson, B. J. (2015). Principal component analysis of Birkeland currents determined by the Active Magnetosphere and Planetary Electrodynamics Response Experiment. *Journal of Geophysical Research: Space Physics*, *120*(12), 10,415–10,424. Retrieved from https://doi.org/10.1002/2015JA021680 doi: 10.1002/2015JA021680

Milan, S. E., Carter, J. A., Sangha, H., Laundal, K. M., Østgaard, N., Tenfjord, P., ... Anderson, B. J. (2018). Timescales of dayside and nightside field-aligned current response to changes in solar wind-magnetosphere coupling. *Journal of Geophysical Research: Space Physics*, *123*(9), 7307-7319. Retrieved from https://agupubs.onlinelibrary.wiley.com/doi/abs/10.1029/2018JA025645

980 doi: https://doi.org/10.1029/2018JA025645

981 Milan, S. E., Clausen, L. B. N., Coxon, J. C., Carter, J. A., Walach, M.-T., Laun-
982 dal, K., ... Anderson, B. J. (2017). Overview of solar wind–magnetosphere–
983 ionosphere–atmosphere coupling and the generation of magnetospheric currents.
984 *Space Science Reviews*, *206*(1), 547–573. Retrieved from `https://doi.org/`
985 `10.1007/s11214-017-0333-0` doi: 10.1007/s11214-017-0333-0

986 Milan, S. E., Grocott, A., Forsyth, C., Imber, S. M., Boakes, P. D., & Hubert, B.
987 (2009). A superposed epoch analysis of auroral evolution during substorm growth,
988 onset and recovery: Open magnetic flux control of substorm intensity. *Annales*
989 *Geophysicae*, *27*(2), 659–668. Retrieved from `http://www.ann-geophys.net/27/`
990 `659/2009/` doi: 10.5194/angeo-27-659-2009

991 Milan, S. E., Hutchinson, J., Boakes, P. D., & Hubert, B. (2009). Influences on the
992 radius of the auroral oval. *Annales Geophysicae*, *27*(7), 2913–2924. Retrieved
993 from `http://www.ann-geophys.net/27/2913/2009/` doi: 10.5194/angeo-27-2913
994 -2009

995 Mishin, V. V., Tsegmed, B., Klibanova, Y. Y., & Kurikalova, M. A. (2020). Burst
996 geomagnetic pulsations as indicators of substorm expansion onsets during storms.
997 *Journal of Geophysical Research: Space Physics*, *125*(10), e2020JA028521. Re-
998 trieved from `https://agupubs.onlinelibrary.wiley.com/doi/abs/10.1029/`
999 `2020JA028521` (e2020JA028521 2020JA028521) doi: https://doi.org/10.1029/
1000 2020JA028521

1001 Morley, S. K., Koller, J., Welling, D. T., Larsen, B. A., Henderson, M. G., & Niehof,
1002 J. T. (2010). SpacePy – a Python-based library of tools for the space sciences.
1003 In S. van der Walt & J. Millman (Eds.), *Proceedings of the 9th Python in Science*
1004 *Conference (SciPy 2010)* (pp. 39–45). Austin, TX.

1005 Murphy, K. R., Mann, I. R., Rae, I. J., Waters, C. L., Anderson, B. J., Milling,
1006 D. K., ... Korth, H. (2012). Reduction in field-aligned currents preceding
1007 and local to auroral substorm onset. *Geophysical Research Letters*, *39*(15).
1008 Retrieved from `https://doi.org/10.1029/2012GL052798` (L15106) doi:
1009 10.1029/2012GL052798

1010 Murphy, K. R., Watt, C. E. J., Mann, I. R., Jonathan Rae, I., Sibeck, D. G., Boyd,
1011 A. J., ... Fennell, J. (2018). The global statistical response of the outer radiation
1012 belt during geomagnetic storms. *Geophysical Research Letters*, *45*(9), 3783-3792.

Retrieved from https://agupubs.onlinelibrary.wiley.com/doi/abs/10.1002/2017GL076674 doi: https://doi.org/10.1002/2017GL076674

Nakamura, R., Sergeev, V. A., Baumjohann, W., Plaschke, F., Magnes, W., Fischer, D., ... Saito, Y. (2016). Transient, small-scale field-aligned currents in the plasma sheet boundary layer during storm time substorms. *Geophysical Research Letters*, *43*(10), 4841–4849. Retrieved from https://doi.org/10.1002/2016GL068768 doi: 10.1002/2016GL068768

Newell, P. T., & Gjerloev, J. W. (2011). Evaluation of SuperMAG auroral electrojet indices as indicators of substorms and auroral power. *Journal of Geophysical Research: Space Physics*, *116*(A12). Retrieved from https://doi.org/10.1029/2011JA016779 doi: 10.1029/2011JA016779

Ohtani, S., Potemra, T. A., Newell, P. T., Zanetti, L. J., Iijima, T., Watanabe, M., ... Woch, J. G. (1995a). Four large-scale field-aligned current systems in the dayside high-latitude region. *Journal of Geophysical Research: Space Physics*, *100*(A1), 137–153. Retrieved from https://doi.org/10.1029/94JA01744 doi: 10.1029/94JA01744

Ohtani, S., Potemra, T. A., Newell, P. T., Zanetti, L. J., Iijima, T., Watanabe, M., ... Blomberg, L. G. (1995b). Simultaneous prenoon and postnoon observations of three field-aligned current systems from Viking and DMSP-F7. *Journal of Geophysical Research: Space Physics*, *100*(A1), 119-136. Retrieved from https://agupubs.onlinelibrary.wiley.com/doi/abs/10.1029/94JA02073 doi: 10.1029/94JA02073

Ovodenko, V. B., Klimenko, M. V., Zakharenkova, I. E., Oinats, A. V., Kotova, D. S., Nikolaev, A. V., ... Chernyshov, A. A. (2020). Spatial and temporal evolution of different-scale ionospheric irregularities in Central and East Siberia during the 27–28 May 2017 geomagnetic storm. *Space Weather*, *18*(6), e2019SW002378. Retrieved from https://agupubs.onlinelibrary.wiley.com/doi/abs/10.1029/2019SW002378 (e2019SW002378) doi: 10.1029/2019SW002378

Pedersen, M. N., Vanhamäki, H., & Aikio, A. T. (2023). Comparison of field-aligned current responses to HSS/SIR, sheath, and magnetic cloud driven geomagnetic storms. *Geophysical Research Letters*, *50*(11), e2023GL103151. Retrieved from https://agupubs.onlinelibrary.wiley.com/doi/abs/10.1029/2023GL103151 doi: https://doi.org/10.1029/2023GL103151

Pedersen, M. N., Vanhamäki, H., Aikio, A. T., Käki, S., Workayehu, A. B., Waters, C. L., & Gjerloev, J. W. (2021). Field-aligned and ionospheric currents by AMPERE and SuperMAG during HSS/SIR-driven storms. *Journal of Geophysical Research: Space Physics*, *126*(11), e2021JA029437. Retrieved from https://agupubs.onlinelibrary.wiley.com/doi/abs/10.1029/2021JA029437 (e2021JA029437 2021JA029437) doi: https://doi.org/10.1029/2021JA029437

Pedersen, M. N., Vanhamäki, H., Aikio, A. T., Waters, C. L., Gjerloev, J. W., Käki, S., & Workayehu, A. B. (2022). Effect of ICME-driven storms on field-aligned and ionospheric currents from AMPERE and SuperMAG. *Journal of Geophysical Research: Space Physics*, *127*(8), e2022JA030423. Retrieved from https://agupubs.onlinelibrary.wiley.com/doi/abs/10.1029/2022JA030423 (e2022JA030423 2022JA030423) doi: https://doi.org/10.1029/2022JA030423

Ridders, C. J. F. (1979). A new algorithm for computing a single root of a real continuous function. *IEEE Transactions on Circuits and Systems*, *26*(11), 979-980. doi: 10.1109/TCS.1979.1084580

Rocklin, M. (2015). Dask: Parallel computation with blocked algorithms and task scheduling. In K. Huff & J. Bergstra (Eds.), *Proceedings of the 14th Python in Science Conference* (p. 130 - 136).

Saunders, M. A. (1989). Origin of the cusp Birkeland currents. *Geophysical Research Letters*, *16*(2), 151-154. Retrieved from https://agupubs.onlinelibrary.wiley.com/doi/abs/10.1029/GL016i002p00151 doi: 10.1029/GL016i002p00151

Sergeev, V. A., Nikolaev, A. V., Kubyshkina, M. V., Tsyganenko, N. A., Singer, H. J., Rodriguez, J. V., ... Korth, H. (2014). Event study combining magnetospheric and ionospheric perspectives of the substorm current wedge modeling. *Journal of Geophysical Research: Space Physics*, *119*(12), 9714–9728. Retrieved from https://doi.org/10.1002/2014JA020522 doi: 10.1002/2014JA020522

Sergeev, V. A., Nikolaev, A. V., Tsyganenko, N. A., Angelopoulos, V., Runov, A. V., Singer, H. J., & Yang, J. (2014). Testing a two-loop pattern of the substorm current wedge (SCW2L). *Journal of Geophysical Research: Space Physics*, *119*(2), 947–963. Retrieved from https://doi.org/10.1002/2013JA019629 doi: 10.1002/2013JA019629

Sergeev, V. A., Tsyganenko, N. A., Smirnov, M. V., Nikolaev, A. V., Singer, H. J., & Baumjohann, W. (2011). Magnetic effects of the substorm current

wedge in a "spread-out wire" model and their comparison with ground, geosynchronous, and tail lobe data. *Journal of Geophysical Research: Space Physics*, *116*(A7). Retrieved from https://doi.org/10.1029/2011JA016471 doi: 10.1029/2011JA016471

Shore, R. M., Freeman, M. P., Coxon, J. C., Thomas, E. G., Gjerloev, J. W., & Olsen, N. (2019). Spatial variation in the responses of the surface external and induced magnetic field to the solar wind. *Journal of Geophysical Research: Space Physics*, *124*(7), 6195-6211. Retrieved from https://agupubs.onlinelibrary.wiley.com/doi/abs/10.1029/2019JA026543 doi: 10.1029/2019JA026543

Siscoe, G. L., & Huang, T. S. (1985). Polar cap inflation and deflation. *Journal of Geophysical Research: Space Physics*, *90*(A1), 543–547. Retrieved from https://doi.org/10.1029/JA090iA01p00543 doi: 10.1029/JA090iA01p00543

Sitnov, M., Birn, J., Ferdousi, B., Gordeev, E., Khotyaintsev, Y., Merkin, V., ... Zhou, X. (2019). Explosive magnetotail activity. *Space Science Reviews*, *215*(4), 31. Retrieved from https://doi.org/10.1007/s11214-019-0599-5 doi: 10.1007/s11214-019-0599-5

Smith, A. W., Forsyth, C., Rae, J., Rodger, C. J., & Freeman, M. P. (2021). The impact of sudden commencements on ground magnetic field variability: Immediate and delayed consequences. *Space Weather*, *19*(7), e2021SW002764. Retrieved from https://agupubs.onlinelibrary.wiley.com/doi/abs/10.1029/2021SW002764 (e2021SW002764 2021SW002764) doi: https://doi.org/10.1029/2021SW002764

Smith, A. W., Freeman, M. P., Rae, I. J., & Forsyth, C. (2019). The influence of sudden commencements on the rate of change of the surface horizontal magnetic field in the United Kingdom. *Space Weather*, *17*(11), 1605-1617. Retrieved from https://agupubs.onlinelibrary.wiley.com/doi/abs/10.1029/2019SW002281 doi: 10.1029/2019SW002281

Sofko, G. J., Greenwald, R., & Bristow, W. (1995). Direct determination of large-scale magnetospheric field-aligned currents with SuperDARN. *Geophysical Research Letters*, *22*(15), 2041–2044. Retrieved from https://doi.org/10.1029/95GL01317 doi: 10.1029/95GL01317

Taylor, J. R., Lester, M., & Yeoman, T. K. (1994). A superposed epoch analysis of geomagnetic storms. *Annales Geophysicae*, *12*(7), 612-624. doi: 10.1007/s00585

-994-0612-4

Tsurutani, B. T., Gonzalez, W. D., Tang, F., & Lee, Y. T. (1992). Great magnetic storms. *Geophysical Research Letters*, *19*(1), 73-76. Retrieved from https://agupubs.onlinelibrary.wiley.com/doi/abs/10.1029/91GL02783 doi: https://doi.org/10.1029/91GL02783

Virtanen, P., Gommers, R., Oliphant, T. E., Haberland, M., Reddy, T., Cournapeau, D., ... SciPy 1.0 Contributors (2020). SciPy 1.0: Fundamental algorithms for scientific computing in Python. *Nature Methods*, *17*, 261–272. doi: 10.1038/s41592-019-0686-2

Walach, M.-T. (2023). *Geomagnetic storm list 1981-2019* [Dataset]. Lancaster University. Retrieved from https://www.research.lancs.ac.uk/portal/en/datasets/geomagnetic-storm-list-19812019(a15ec887-f955-4d6c-ac65-30c9a27c8a58).html doi: 10.17635/lancaster/researchdata/622

Walach, M.-T., & Grocott, A. (2019). SuperDARN observations during geomagnetic storms, geomagnetically active times, and enhanced solar wind driving. *Journal of Geophysical Research: Space Physics*, *124*(7), 5828-5847. Retrieved from https://agupubs.onlinelibrary.wiley.com/doi/abs/10.1029/2019JA026816 doi: https://doi.org/10.1029/2019JA026816

Walach, M.-T., & Milan, S. E. (2015). Are steady magnetospheric convection events prolonged substorms? *Journal of Geophysical Research: Space Physics*, *120*(3), 1751-1758. Retrieved from https://agupubs.onlinelibrary.wiley.com/doi/abs/10.1002/2014JA020631 doi: https://doi.org/10.1002/2014JA020631

Walach, M.-T., Milan, S. E., Murphy, K. R., Carter, J. A., Hubert, B. A., & Grocott, A. (2017). Comparative study of large-scale auroral signatures of substorms, steady magnetospheric convection events, and sawtooth events. *Journal of Geophysical Research: Space Physics*, *122*(6), 6357-6373. Retrieved from https://agupubs.onlinelibrary.wiley.com/doi/abs/10.1002/2017JA023991 doi: https://doi.org/10.1002/2017JA023991

Waters, C. L., Anderson, B. J., Green, D. L., Korth, H., Barnes, R. J., & Vanhamäki, H. (2020). Science data products for AMPERE. In M. W. Dunlop & H. Lühr (Eds.), *Ionospheric multi-spacecraft analysis tools: Approaches for deriving ionospheric parameters* (pp. 141–165). Cham: Springer International Publishing. Retrieved from https://doi.org/10.1007/978-3-030-26732-2_7

doi: 10.1007/978-3-030-26732-2_7

Waters, C. L., Anderson, B. J., & Liou, K. (2001). Estimation of global field-aligned currents using the Iridium System magnetometer data. *Geophysical Research Letters*, *28*(11), 2165–2168. Retrieved from https://doi.org/10.1029/2000GL012725 doi: 10.1029/2000GL012725

Weimer, D. R. (2001). Maps of ionospheric field-aligned currents as a function of the interplanetary magnetic field derived from Dynamics Explorer 2 data. *Journal of Geophysical Research: Space Physics*, *106*(A7), 12889–12902. Retrieved from https://doi.org/10.1029/2000JA000295 doi: 10.1029/2000JA000295

Yokoyama, N., & Kamide, Y. (1997). Statistical nature of geomagnetic storms. *Journal of Geophysical Research: Space Physics*, *102*(A7), 14215-14222. Retrieved from https://agupubs.onlinelibrary.wiley.com/doi/abs/10.1029/97JA00903 doi: https://doi.org/10.1029/97JA00903

Zanetti, L. J., Potemra, T. A., Iijima, T., Baumjohann, W., & Bythrow, P. F. (1984). Ionospheric and Birkeland current distributions for northward interplanetary magnetic field: Inferred polar convection. *Journal of Geophysical Research: Space Physics*, *89*(A9), 7453–7458. Retrieved from https://doi.org/10.1029/JA089iA09p07453 doi: 10.1029/JA089iA09p07453